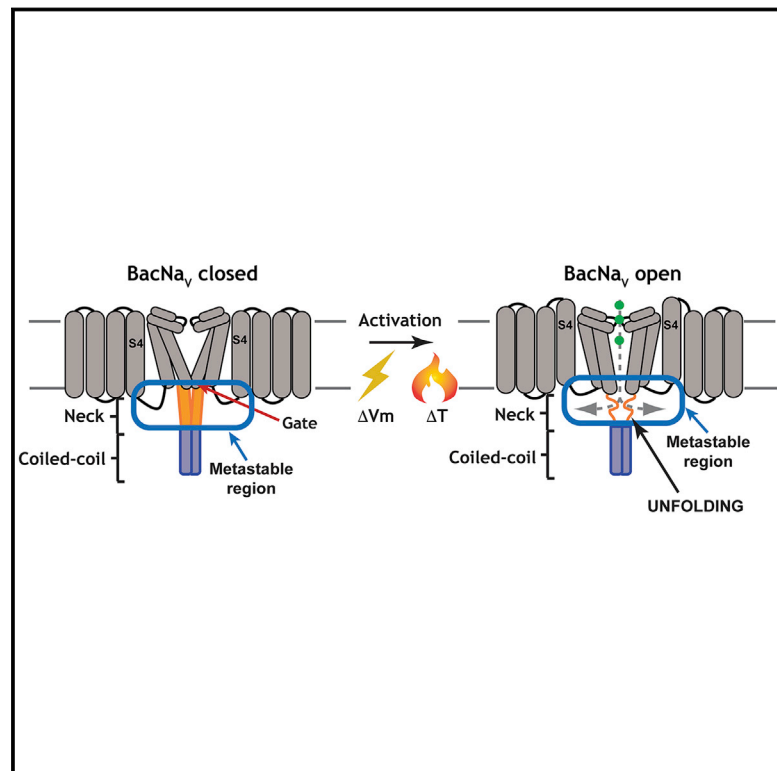


Unfolding of a Temperature-Sensitive Domain Controls Voltage-Gated Channel Activation

Graphical Abstract



Authors

Cristina Arrigoni, Ahmed Rohaim, David Shaya, ..., Smriti Mishra, Hassane S. Mchaourab, Daniel L. Minor, Jr.

Correspondence

daniel.minor@ucsf.edu

In Brief

A cytoplasmic domain of bacterial sodium channels controls channel gating directly through a temperature-dependent reversible structural transition in a metastable region proximal to the pore.

Highlights

- The BacNa_v cytoplasmic domain has profound effects on voltage-dependent gating
- An unfolding transition in the cytoplasmic domain metastable hydrophilic core tunes BacNa_v gating
- BacNa_v cytoplasmic domain unfolding is localized and temperature dependent
- A discrete domain can encode the temperature-dependent response of a channel

Accession Numbers

5HJ8
5HK6
5HKD
5HK7
5HKT
5HKU



Unfolding of a Temperature-Sensitive Domain Controls Voltage-Gated Channel Activation

Cristina Arrigoni,^{1,8} Ahmed Rohaim,^{1,7,8} David Shaya,¹ Felix Findeisen,¹ Richard A. Stein,⁶ Shailika Reddy Nurva,¹ Smriti Mishra,⁶ Hassane S. Mchaourab,⁶ and Daniel L. Minor, Jr.^{1,2,3,4,5,*}

¹Cardiovascular Research Institute

²Department of Biochemistry and Biophysics

³Department of Cellular and Molecular Pharmacology

⁴California Institute for Quantitative Biomedical Research

University of California, San Francisco, San Francisco, CA 94158, USA

⁵Physical Biosciences Division, Lawrence Berkeley National Laboratory, Berkeley, CA 94720, USA

⁶Department of Molecular Physiology and Biophysics, Vanderbilt University, Nashville, TN 37232, USA

⁷Department of Biophysics, Faculty of Science, Cairo University, Giza, Egypt

⁸Co-first author

*Correspondence: daniel.minor@ucsf.edu

<http://dx.doi.org/10.1016/j.cell.2016.02.001>

SUMMARY

Voltage-gated ion channels (VGICs) are outfitted with diverse cytoplasmic domains that impact function. To examine how such elements may affect VGIC behavior, we addressed how the bacterial voltage-gated sodium channel (BacNa_v) C-terminal cytoplasmic domain (CTD) affects function. Our studies show that the BacNa_v CTD exerts a profound influence on gating through a temperature-dependent unfolding transition in a discrete cytoplasmic domain, the neck domain, proximal to the pore. Structural and functional studies establish that the BacNa_v CTD comprises a bi-partite four-helix bundle that bears an unusual hydrophilic core whose integrity is central to the unfolding mechanism and that couples directly to the channel activation gate. Together, our findings define a general principle for how the widespread four-helix bundle cytoplasmic domain architecture can control VGIC responses, uncover a mechanism underlying the diverse BacNa_v voltage dependencies, and demonstrate that a discrete domain can encode the temperature-dependent response of a channel.

INTRODUCTION

Cells shape their electrical activity by controlling ion channel function in response to physical and chemical cues. Voltage-gated ion channels (VGICs) are exquisitely sensitive to transmembrane potential changes by virtue of a voltage-sensor domain that is embedded in the membrane bilayer (Vargas et al., 2012; Yu et al., 2005). Beyond the intrinsic ability to detect transmembrane voltage changes, VGIC superfamily members possess diverse intracellular domains (Yu et al., 2005) that are employed to tune voltage-dependent responses of a particular channel as a consequence of stimuli from signaling molecules

(Morais-Cabral and Robertson, 2015; Yang et al., 2015). Although such domains provide a means for chemical cues to influence VGICs, the sensitivity to physical stimuli, such as temperature, in some VGIC superfamily members (Schneider et al., 2014; Vriens et al., 2014), has raised the question about whether there are equivalently specialized domains that can serve as temperature sensors (Bagriantsev et al., 2012; Brauchi et al., 2006; Grandl et al., 2008) or whether thermal responses arise from elements distributed throughout the channel (Chowdhury et al., 2014; Clapham and Miller, 2011). Moreover, despite notable advances in understanding the structures of some VGIC regulatory domains that respond to ligand or regulatory protein modulation (Jiang et al., 2002; Pioletti et al., 2006; Yuan et al., 2010; Zagotta et al., 2003), how conformational changes within these domains impact the channel pore and alter function remains incompletely understood.

Bacterial voltage-gated sodium channels (BacNa_vs) share the six-transmembrane VGIC superfamily architecture and bear a four-helix bundle C-terminal cytoplasmic domain (CTD) that terminates in a four-stranded coiled-coil (Irie et al., 2012; Mio et al., 2010; Payandeh and Minor, 2015; Powl et al., 2010; Shaya et al., 2014). BacNa_vs display remarkably diverse voltage responses (Payandeh and Minor, 2015; Scheuer, 2014), having activation potentials, $V_{1/2}$, that span an ~120 mV range (Scheuer, 2014), from -98 mV for Na_vAb from *Arcobacter butzleri* (Payandeh et al., 2012) to +27 mV for Na_vSp1 from *Silicibacter pomeroyi* (Shaya et al., 2014). The structural basis for this wide voltage response range is unknown (Scheuer, 2014). The CTD domain proximal to the channel pore termed the “neck” is the most diverse element (Payandeh and Minor, 2015; Powl et al., 2010; Shaya et al., 2014) and appears to adopt varied degrees of structure in different BacNa_vs (Bagn  ris et al., 2013; Shaya et al., 2014; Tsai et al., 2013). Studies of different BacNa_vs indicate that the CTD is important for assembly (Bagn  ris et al., 2013; Mio et al., 2010; Powl et al., 2010; Tsai et al., 2013) and function (Bagn  ris et al., 2013; Irie et al., 2012; Shaya et al., 2014; Tsai et al., 2013). Nevertheless, a clear consensus for the mechanism by which the CTD influences channel function and the means by which it might influence the channel pore remains unknown.

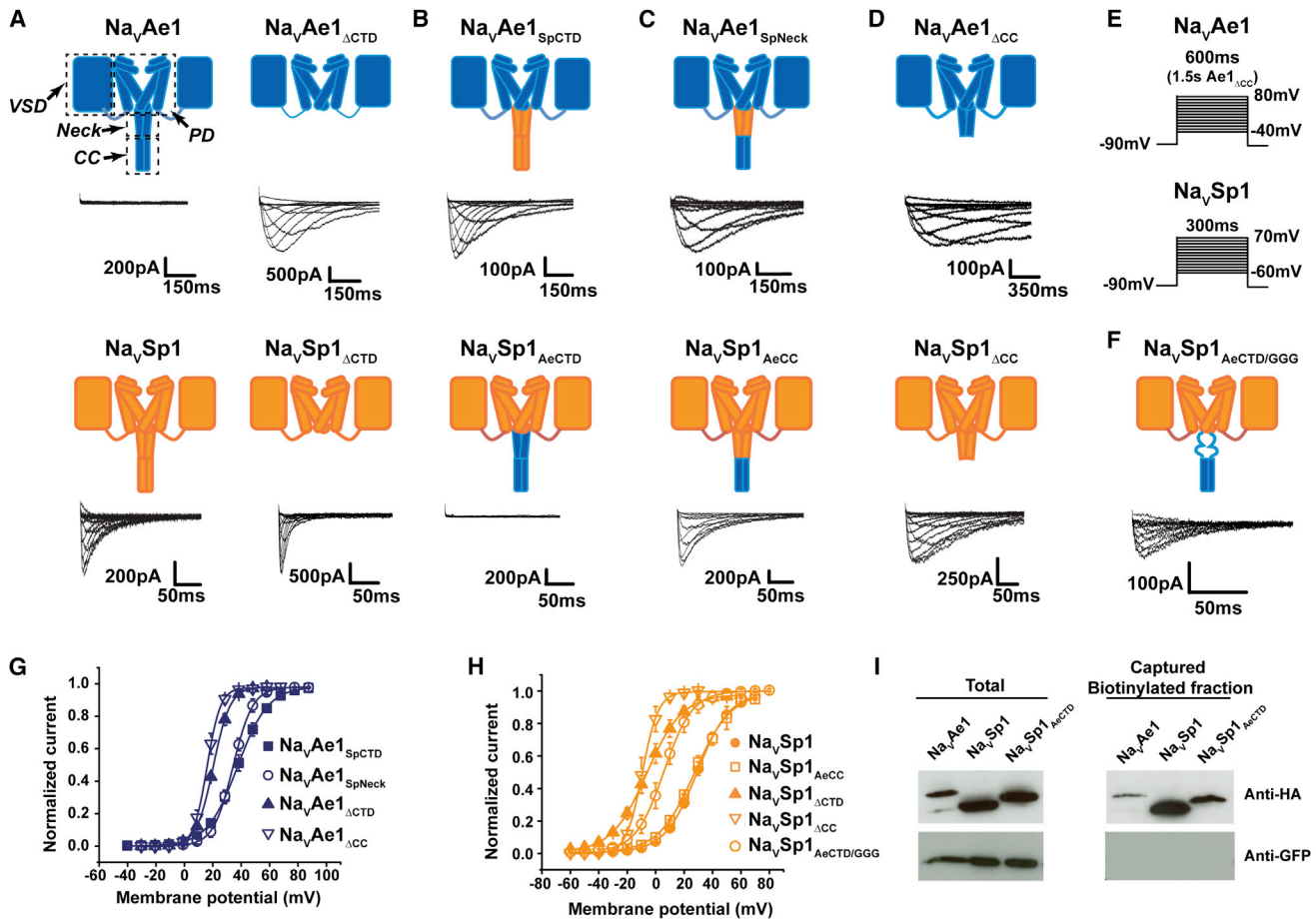


Figure 1. BacNa_V CTD Affects Function

(A–D) Functional comparison of (A) $\text{Na}_V\text{Ae1}$, $\text{Na}_V\text{Sp1}$, $\text{Na}_V\text{Ae1}_{\Delta\text{CTD}}$, and $\text{Na}_V\text{Sp1}_{\Delta\text{CTD}}$; (B) $\text{Na}_V\text{Ae1}_{\text{SpCTD}}$ and $\text{Na}_V\text{Sp1}_{\text{AeCTD}}$; (C) $\text{Na}_V\text{Ae1}_{\text{SpNeck}}$ and $\text{Na}_V\text{Sp1}_{\text{AeCC}}$; and (D) $\text{Na}_V\text{Ae1}_{\Delta\text{CC}}$ and $\text{Na}_V\text{Sp1}_{\Delta\text{CC}}$. Cartoons depict two BacNa_V subunits. Voltage-sensor domain (VSD), pore domain (PD), neck, and coiled-coil (CC) are labeled. $\text{Na}_V\text{Ae1}$ and $\text{Na}_V\text{Sp1}$ elements are blue and orange, respectively.

(E) Voltage protocols for $\text{Na}_V\text{Ae1}$ (top), $\text{Na}_V\text{Sp1}$ (bottom), and chimeras.

(F) $\text{Na}_V\text{Sp1}_{\text{AeCTD}/\text{GGG}}$ exemplar currents.

(G and H) Voltage-dependent activation curves for (G) $\text{Na}_V\text{Ae1}$, $\text{Na}_V\text{Ae1}_{\text{SpCTD}}$, $\text{Na}_V\text{Ae1}_{\text{SpNeck}}$, $\text{Na}_V\text{Ae1}_{\Delta\text{CTD}}$, and $\text{Na}_V\text{Ae1}_{\Delta\text{CC}}$, and (H) $\text{Na}_V\text{Sp1}$, $\text{Na}_V\text{Sp1}_{\text{AeCC}}$, $\text{Na}_V\text{Sp1}_{\Delta\text{CTD}}$, and $\text{Na}_V\text{Sp1}_{\Delta\text{CC}}$.

(I) Western blot of the total lysate and surface-biotinylated fraction for the indicated constructs probed using the specified antibodies.

See also Figure S1 and Table S1.

Here, we show that the BacNa_V CTD has an integral role in controlling channel voltage-dependent behavior and that variation in neck composition and structure cause functional diversity. Moreover, we demonstrate that the neck has a temperature-dependent unfolding transition that is directly coupled to channel opening. These results establish that a discrete ion channel domain can serve as a temperature response element. The BacNa_V CTD location is shared with many VGIC superfamily member helical bundle domains (Howard et al., 2007; Paulsen et al., 2015; Uysal et al., 2009; Wiener et al., 2008; Yu et al., 2012), including channels not principally gated by voltage. This architectural commonality suggests that the principles uncovered here set a framework for understanding how four-helix bundle CTDs can modulate VGIC superfamily member function.

RESULTS

BacNa_V Cytosolic Domain Regulates Voltage-Dependent Channel Opening

To probe BacNa_V CTD function, we focused on two BacNa_Vs having different activation signatures, *Alkallimnicola ehrlichii* $\text{Na}_V\text{Ae1}$ and *Silicibacter pomeroyi* $\text{Na}_V\text{Sp1}$. $\text{Na}_V\text{Sp1}$ displays robust voltage-dependent activity (Koishi et al., 2004; Shaya et al., 2014), whereas $\text{Na}_V\text{Ae1}$ has not yielded functional data unless neck mutations are present (Shaya et al., 2014) (Figure 1A). We deleted the $\text{Na}_V\text{Ae1}$ and $\text{Na}_V\text{Sp1}$ CTDs at the hinge between the pore module and CTD (ending at $\text{Na}_V\text{Ae1}$ His245 and $\text{Na}_V\text{Sp1}$ His224, respectively) (Figure S1A) (Shaya et al., 2014). Contrary to the loss of function reported for other BacNa_V CTD deletions (Mio et al., 2010; Tsai et al., 2013), $\text{Na}_V\text{Ae1}_{\Delta\text{CTD}}$ and $\text{Na}_V\text{Sp1}_{\Delta\text{CTD}}$

produced robust voltage-dependent currents, demonstrating that CTD removal did not strongly affect folding or tetramerization (Figure 1A). However, CTD deletion had robust effects on voltage-dependent activation, causing large left shifts in $V_{1/2}$ relative to the references ($V_{1/2} = 19.1 \pm 1.9$ and 32.1 ± 1.1 mV, for $\text{Na}_v\text{Ae1}_{\Delta\text{CTD}}$ and a functional mutant bearing a neck triple glycine substitution $\text{Na}_v\text{Ae1}_{\text{GGG}}$ [Shaya et al., 2014], respectively, and -7.4 ± 2.8 and 28.9 ± 1.3 , for $\text{Na}_v\text{Sp1}_{\Delta\text{CTD}}$ and $\text{Na}_v\text{Sp1}$, respectively) (Figures 1G and 1H; Table S1). Thus, CTD deletion produces $\text{Na}_v\text{Ae1}$ and $\text{Na}_v\text{Sp1}$ channels that are more readily opened by voltage.

The CTD has two parts, the neck (Payandeh and Minor, 2015; Shaya et al., 2014), proximal to the transmembrane pore, and a C-terminal four stranded coiled-coil (Irie et al., 2012; Mio et al., 2010; Payandeh and Minor, 2015; Powl et al., 2010; Shaya et al., 2014). Because CTD deletion had such a strong effect on $\text{Na}_v\text{Ae1}$ and $\text{Na}_v\text{Sp1}$ function, we created a series of chimeras (Figure S1A) to define whether the effects caused by the CTD arise from the neck, coiled-coil, or both. CTD exchange between $\text{Na}_v\text{Ae1}$ and $\text{Na}_v\text{Sp1}$ yielded channels, $\text{Na}_v\text{Ae1}_{\text{SpCTD}}$ and $\text{Na}_v\text{Sp1}_{\text{AeCTD}}$, that phenocopied the properties of the CTD parent; $\text{Na}_v\text{Ae1}_{\text{SpCTD}}$ was functional ($V_{1/2} = 38.8 \pm 2.5$ mV) whereas $\text{Na}_v\text{Sp1}_{\text{AeCTD}}$ showed no activity (Figure 1B; Table S1). Exchanging the $\text{Na}_v\text{Ae1}$ coiled-coil into $\text{Na}_v\text{Ae1}_{\text{SpCTD}}$ to make an $\text{Na}_v\text{Ae1}$ chimera bearing the $\text{Na}_v\text{Sp1}$ neck and $\text{Na}_v\text{Ae1}$ coiled-coil, $\text{Na}_v\text{Ae1}_{\text{SpNeck}}$, produced a channel having voltage-dependent gating that was essentially identical to $\text{Na}_v\text{Ae1}_{\text{SpCTD}}$ ($V_{1/2} = 32.7 \pm 2.0$ and 38.8 ± 2.5 mV for $\text{Na}_v\text{Ae1}_{\text{SpNeck}}$ and $\text{Na}_v\text{Ae1}_{\text{SpCTD}}$, respectively) (Figures 1C and 1G; Table S1). Substitution of the $\text{Na}_v\text{Sp1}$ neck into $\text{Na}_v\text{Sp1}_{\text{AeCTD}}$ produced a $\text{Na}_v\text{Sp1}$ chimera having the $\text{Na}_v\text{Ae1}$ coiled-coil, $\text{Na}_v\text{Sp1}_{\text{AeCC}}$ that displayed voltage-dependent gating identical to $\text{Na}_v\text{Sp1}$ ($V_{1/2} = 26.1 \pm 1.0$ and 28.9 ± 1.3 mV, for $\text{Na}_v\text{Sp1}_{\text{AeCC}}$ and $\text{Na}_v\text{Sp1}$ respectively) (Figures 1C and 1H; Table S1). Taken together, these results demonstrate that coiled-coil identity has minimal functional effects, and the neck is the principal source of the differences in $\text{Na}_v\text{Ae1}$ and $\text{Na}_v\text{Sp1}$ voltage-dependent behaviors. Although the coiled-coil did not influence channel voltage-dependent properties, it seemed possible that its ability to constrain the neck C-terminal end might be important for the neck to affect gating. Therefore, we examined $\text{Na}_v\text{Ae1}$ and $\text{Na}_v\text{Sp1}$ mutants in which the neck was intact but the coiled-coil was deleted, $\text{Na}_v\text{Ae1}_{\Delta\text{CC}}$ and $\text{Na}_v\text{Sp1}_{\Delta\text{CC}}$. Both yielded channels having a $V_{1/2}$ indistinguishable from complete CTD deletion (19.1 ± 1.9 and 17.4 ± 1.7 mV for $\text{Na}_v\text{Ae1}_{\Delta\text{CC}}$ and $\text{Na}_v\text{Ae1}_{\Delta\text{CTD}}$; -7.4 ± 2.8 and -9.7 ± 1.9 mV for $\text{Na}_v\text{Sp1}_{\Delta\text{CC}}$ and $\text{Na}_v\text{Sp1}_{\Delta\text{CTD}}$, respectively) (Figures 1D, 1G, and 1H; Table S1). Thus, together with the chimera results, these data indicate that the coiled-coil is required to constrain the C-terminal end of the neck, although its identity has minimal effect on function.

Because we were unable to measure currents from $\text{Na}_v\text{Ae1}$ and $\text{Na}_v\text{Sp1}_{\text{AeCTD}}$ (Figures 1A and 1B), channels that have a wild-type $\text{Na}_v\text{Ae1}$ neck, we tested whether these proteins had plasma membrane expression to resolve whether the lack of activity came from an absence of surface expression or from channels that could not be opened. We placed an N-terminal hemagglutinin (HA) tag on $\text{Na}_v\text{Ae1}$, $\text{Na}_v\text{Sp1}_{\text{AeCTD}}$, and $\text{Na}_v\text{Sp1}$ and used a surface biotinylation assay to assess plasma

membrane expression. Streptavidin capture of the surface-biotinylated fraction followed by anti-HA antibody detection showed clear signals for all three channels. By contrast, this fraction had no signal for the intracellular control, GFP, when probed with an anti-GFP antibody. Thus, the non-functional channels, $\text{Na}_v\text{Ae1}$ and $\text{Na}_v\text{Sp1}_{\text{AeCTD}}$, are indeed expressed on the plasma membrane (Figure 1I). Moreover, similar to the effects on $\text{Na}_v\text{Ae1}$ (Shaya et al., 2014), inclusion of a triple-glycine substitution in the neck domain of $\text{Na}_v\text{Sp1}_{\text{AeCTD}}$ generated a functional channel ($\text{Na}_v\text{Sp1}_{\text{AeCTD}/\text{GGG}}$ $V_{1/2} = 5.75 \pm 2.6$ mV; Figures 1F and 1H; Table S1). Together with the results of the chimeras and previous neck mutants (Shaya et al., 2014), these findings suggest that $\text{Na}_v\text{Ae1}$ and $\text{Na}_v\text{Sp1}_{\text{AeCTD}}$ fail to produce currents because the $\text{Na}_v\text{Ae1}$ neck produces a $V_{1/2}$ that is outside of the measureable voltage range of our experiments.

Our data demonstrate that the CTD functions as a regulatory module whose intrinsic properties enable it to exert diverse effects on BacNa_v voltage-dependent gating. The neck influence is strong on voltage-dependent activation and contrasts with its modest effects on voltage-dependent inactivation (Figures 1, S1B, and S1C; Table S1), a process for which the pore domain is important (Pavlov et al., 2005; Payandeh et al., 2012; Shaya et al., 2014). Thus, our investigations establish that the origins of the dramatic modulation of voltage-dependent gating reside in the neck and require the neck to be constrained at the C-terminal end by the coiled-coil domain.

Diverse BacNa_v CTDs Alter $\text{Na}_v\text{Sp1}$ Transmembrane Domain Voltage Responses

Prior functional studies reported BacNa_v $V_{1/2}$ activation values spanning an ~ 120 mV range (Koishi et al., 2004; Payandeh et al., 2012; Ren et al., 2001; Shaya et al., 2014; Ulmschneider et al., 2013). The source of this diversity has been unclear (Scheuer, 2014). Given the profound effects of the CTD on $\text{Na}_v\text{Sp1}$ and $\text{Na}_v\text{Ae1}$, we next asked how replacement of the $\text{Na}_v\text{Sp1}$ CTD with CTDs from previously studied BacNa_v s having diverse lengths and compositions would affect function: $\text{Na}_v\text{Bh1}$ ($\text{Na}_v\text{Sp1}_{\text{BHCTD}}$), Na_vMs ($\text{Na}_v\text{Sp1}_{\text{MsCTD}}$), Na_vAb ($\text{Na}_v\text{Sp1}_{\text{AbCTD}}$), $\text{Na}_v\text{Ab1}$ (Shaya et al., 2011) ($\text{Na}_v\text{Sp1}_{\text{Ab1CTD}}$), and Na_vPz ($\text{Na}_v\text{Sp1}_{\text{PzCTD}}$) (Figures 2A and S1A). In whole cell recordings, each of these channels, except $\text{Na}_v\text{Sp1}_{\text{AbCTD}}$, was functional (Figure 2B). Strikingly, the CTD substitutions had diverse effects ranging from little change in voltage-dependent activation relative to $\text{Na}_v\text{Sp1}$ for the Na_vPz CTD ($\Delta V_{1/2} = -4.2$ mV) to producing large voltage-dependent activation shifts in both the negative ($\Delta V_{1/2} = -44.5 \pm 4.4$ and -27.3 ± 3.8 mV, $\text{Na}_v\text{Bh1}$ and Na_vMs CTDs, respectively) and positive directions ($\Delta V_{1/2} = +20.4 \pm 5.8$ mV $\text{Na}_v\text{Ab1}$ CTD) (Figure 2C; Table S1). For the $\text{Na}_v\text{Sp1}_{\text{BHCTD}}$, the activation threshold was similar to that of $\text{Na}_v\text{Sp1}_{\Delta\text{CTD}}$ ($\Delta V_{1/2} = -44.5 \pm 4.4$ mV and -36.3 ± 5.4 mV, respectively), a result that is in line with data suggesting that the $\text{Na}_v\text{Bh1}$ neck is disordered (Powl et al., 2010) and the observation that $\text{Na}_v\text{Bh1}$ coiled-coil deletion results in channels having voltage-dependent activation indistinguishable from wild-type (Mio et al., 2010). By contrast, the CTD swaps had a more modest effect on voltage-dependent inactivation (Figure S1D; Table S1).

The varied effects of the different CTD chimeras on the voltage-dependence of the $\text{Na}_v\text{Sp1}$ transmembrane core demonstrate

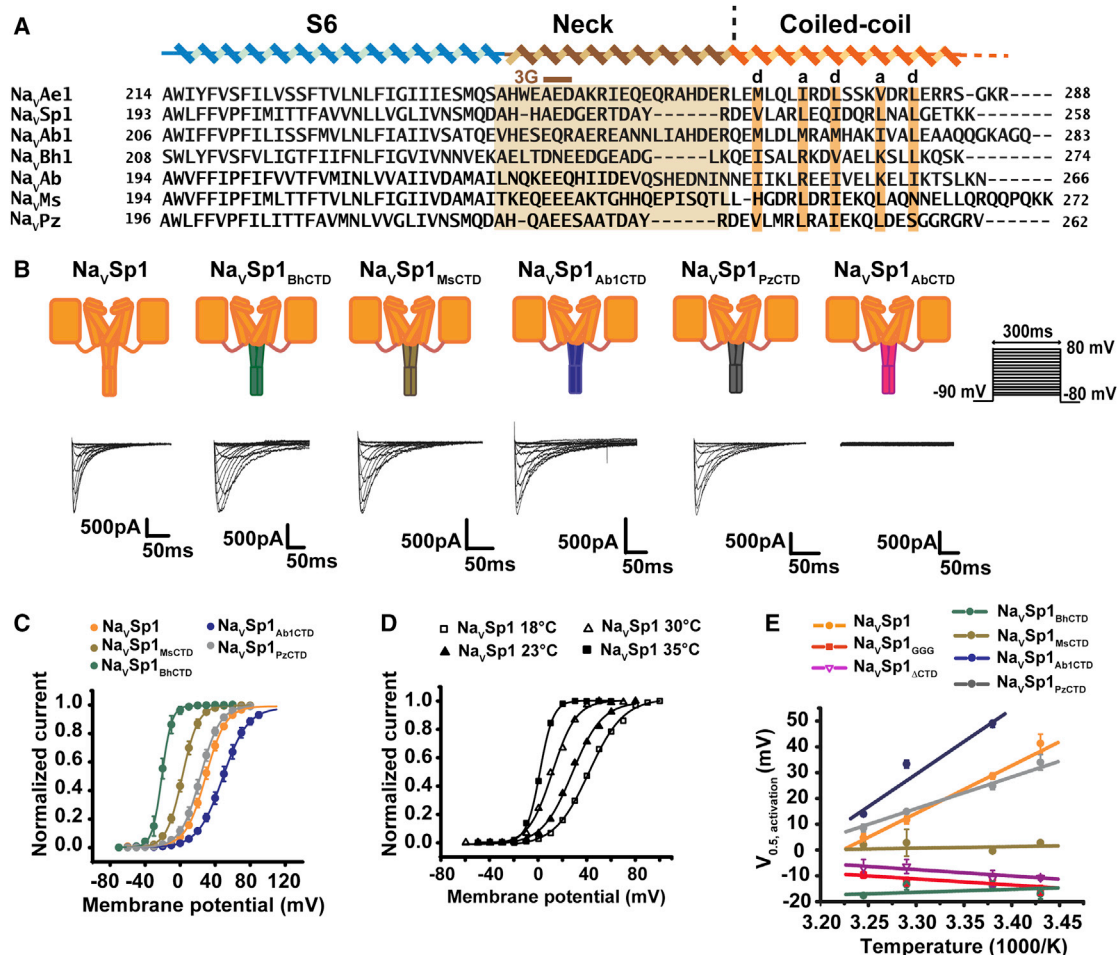


Figure 2. CTD Chimeras Alter Na_vSp1 Voltage-Dependence

(A) Sequence alignment of Na_vAe1, *Alkalinimnicola ehrlichii* (Shaya et al., 2011, 2014), Na_vSp1, *Silicibacter pomeroyi* (Koishi et al., 2004; Shaya et al., 2011); Na_vAb1, *Alcanivorax borkumensis* (Shaya et al., 2011); Na_vBh1 (NaChBac), *Bacillus halodurans* (Ren et al., 2001); Na_vAb, *Arcobacter butzleri* (Payandeh et al., 2011); Na_vMs, *Magnetococcus* sp. (McCusker et al., 2012); and Na_vPz, *Paracoccus zeaxanthinifaciens* (Koishi et al., 2004). S6, neck, coiled-coil “a”-“d” positions, and 3G mutation site are indicated.

(B) Na_vSp1, Na_vSp1_{BhCTD}, Na_vSp1_{MsCTD}, Na_vSp1_{Ab1CTD}, Na_vSp1_{PzCTD}, and Na_vSp1_{AbCTD} exemplar currents and voltage protocol. Cartoons depict two channel subunits.

(C) Activation curves for (B).

(D) Temperature-dependence of Na_vSp1 activation.

(E) $V_{1/2}$ temperature-dependence for the indicated channels. Lines show linear fit.

See also Figures S1 and S2 and Tables S1 and S2.

that each BacNa_v CTD has a distinct effect on channel activation (Figure 2B) and that a simple BacNa_v CTD transplant can tune the voltage-dependence of activation of the transmembrane core over a wide range, ~65 mV (Figure 2C). These results, taken together with the experiments indicating the clear involvement of the BacNa_v neck in channel function (Figure 1) and lack of sensitivity to coiled-coil identity (Figure 1C), strongly support a critical role for the neck in BacNa_v gating. Although specific elements of the BacNa_v transmembrane domains, such as the voltage sensors, must set some of the channel voltage-dependent properties, our findings together with the observation that the neck is the most variable BacNa_v feature (Payandeh and Mi-

nor, 2015), indicate that much of the observed variety in BacNa_v voltage-dependences originates from the neck region. These domains display varied degrees of structure from disordered (Bag-nérís et al., 2013; Powl et al., 2010) to completely ordered (Shaya et al., 2014). Thus, our data points to a common mechanism for tuning voltage dependencies within the BacNa_v family based on the ability of the neck to adopt structure.

Temperature-Dependent Change in the BacNa_v Neck Affects Gating

Previous studies suggested that the neck undergoes an order → disorder transition during channel opening (Shaya et al., 2014)

and pose a hypothesis that predicts very different temperature dependences for BacNa_vs in which the neck is stably folded structure versus those in which it is disordered. To test this, we first examined whether Na_vSp1 voltage-dependent activation was temperature-dependent and whether this response could be influenced by neck properties. The $V_{1/2}$ of Na_vSp1 activation showed a clear temperature dependence, moving ~35 mV in the hyperpolarized direction as temperature increased from 18° to 35°C (Figures 2D and 2E; Table S2). This response was eliminated by increasing the neck flexibility with a triple glycine substitution, Na_vSp1_{GGG} (Shaya et al., 2014), or by CTD deletion, Na_vSp1_{ΔCTD} (Figure 2E; Table S2), supporting the idea that neck structure is crucial for temperature-dependent gating changes.

Because the Na_vSp1 CTD chimeras displayed diverse activation $V_{1/2}$ values (Figure 2C), we next probed whether these CTD substitutions affected channel temperature responses. The chimeras having CTDs bearing disordered necks, Na_vSp1_{BhCTD} and Na_vSp1_{MsCTD} (Bagn eris et al., 2013; Powl et al., 2010), yielded channels that lacked a temperature response in activation $V_{1/2}$ (Figure 2E; Table S2). By contrast, the activation $V_{1/2}$ of Na_vSp1_{PzCTD} and Na_vSp1_{Ab1CTD} showed clear temperature dependence. This response was similar in magnitude to Na_vSp1 (Figure 2E) and shows that the role of the CTD in setting channel temperature-dependent properties is general.

Finally, we examined whether the $V_{1/2}$ changes caused by the CTD substitutions were related to neck structure by examining the consequences of neck triple glycine mutations in Na_vSp1_{MsCTD}, Na_vSp1_{Ab1CTD}, and Na_vSp1_{PzCTD} (Figures S2A and S2B). Neck disruption had no effect on the activation $V_{1/2}$ for the chimera having a disordered neck, Na_vSp1_{MsCTD} ($\Delta V_{1/2}$ = 0.9 mV Na_vSp1_{MsCTD/GGG} relative to Na_vSp1_{MsCTD}) (Figure S2C; Table S1). However, for both chimeras having a temperature-dependent $V_{1/2}$ similar to Na_vSp1, Na_vSp1_{PzCTD} and Na_vSp1_{Ab1CTD}, the GGG mutation caused a large activation $V_{1/2}$ left-shift ($\Delta V_{1/2}$ = -39.3 and -47.2 mV, respectively, for Na_vSp1_{PzCTD} and Na_vSp1_{Ab1CTD}, relative to the parent chimeras) (Figures S2D and S2E; Table S1). This magnitude change is similar to that in Na_vSp1_{GGG} ($\Delta V_{1/2}$ = -39.4 mV) (Figure S2F; Table S1). Given that the triple glycine mutation eliminates Na_vSp1 temperature-dependence, these data suggest that the modulatory effects on $V_{1/2}$ and the temperature-dependent gating properties in Na_vSp1_{PzCTD} and Na_vSp1_{Ab1CTD} arise from neck domain order. Taken together, our data strongly support the hypothesis that a protein unfolding transition in the neck domain is coupled to channel opening and demonstrate that a discrete channel domain can act as a temperature sensor.

Structures of Na_vAe1p Neck Mutants Reveal Disordered Neck and Closed Pore

To define the structural consequences of polyglycine mutations intended to disrupt the neck, we determined crystal structures of two neck domain mutants of “pore-only” channel Na_vAe1p (Shaya et al., 2014), Na_vAe1p-3G and Na_vAe1p-7G, at 3.70 Å and 3.80 Å resolution, respectively (Figures 3A–3D and S3; Table S3). Molecular replacement using the Na_vAe1p transmembrane portion (Shaya et al., 2014) yielded maps having well-defined electron density for the transmembrane regions and part of the

CTDs (Figures S4A and S4B). Model building and refinement showed traceable density for residues that comprise the neck C-terminal ends and complete coiled-coils (Na_vAe1p-3G Ile254-Arg283 and Na_vAe1p-7G Glu257-Arg283) (Figures 3A and 3B) but lacked density for the polyglycines and residues that frame these substitutions (Na_vAe1p-3G Ser243-Arg253 and Na_vAe1p-7G Ser243-Gln256). This localized loss of structure confirms the increase in neck flexibility and shows that the disruption propagates beyond the polyglycines (Figure 3D).

Although the Na_vAe1p-3G and Na_vAe1p-7G necks lack structure, both CTD coiled-coils remained intact. These were displaced from the channel central axis by ~28° (Figure 3C) and in agreement with its increased disorder, this displacement was larger for Na_vAe1p-7G and included a ~8 Å movement toward the pore (Figure 3C). Once the neck is disrupted, the pore domain and coiled-coil appear to be independent. We anticipate that free from the crystal lattice constraints, the coiled-coil could move independently relative to the pore as solution studies suggest (Bagn eris et al., 2013). The fact that the neck disruption does not propagate into the coiled-coil agrees with our observation that coiled-coil identity is not crucial for function but that its presence is essential for the neck to affect function (Figures 1C and 1D).

Although the 3G and 7G substitutions make full-length BacNa_vs easier to open, Na_vAe1p-3G and Na_vAe1p-7G pore domains are closed and match the Na_vAe1p closed structure (Figure S4C) (Shaya et al., 2014) (root-mean-square deviation [RMSD]_{C α} of 0.67 Å and 0.73 Å, respectively). Assignment of a closed conformation is further supported by anomalous difference maps of selenomethionine substituted Na_vAe1p-3G (Figure S4D; Table S3) that reveal clear density on the pore domain central axis for the seleniums of the activation gate residue, Met241 (Shaya et al., 2014). Na_vAe1p-3G and Na_vAe1p-7G structures also revealed density in the selectivity filter “site 2” position (Tang et al., 2014) (Figures S4E–S4G) that we modeled as a calcium atom based on anomalous density (Figure S4F) and the presence of calcium in the crystallization conditions.

As there is no structure of Na_vSp1 or the “pore-only” Na_vSp1p (Shaya et al., 2011), we turned to circular dichroism (CD) spectroscopy to test whether the Na_vAe1p-3G and Na_vAe1p-7G structural changes had parallels in Na_vSp1p. Na_vAe1p, Na_vAe1p-3G, and Na_vAe1p-7G CD spectra showed classic helical features of minima at 208 and 222 nm (Berova et al., 2000). Notably, the intensity of these minima was reduced in Na_vAe1p-3G and Na_vAe1p-7G in an order that matched the crystal structures and was reduced farther by CTD deletion in Na_vAe1p- Δ CTD (Figure 3E). Comparison of the CD spectra of Na_vSp1p (Shaya et al., 2011) with Na_vSp1p-3G showed a similar loss of helical structure (Figures 3D and 3F). To test whether neck disruption affected the thermal stability, we measured the temperature dependence of the CD signal at 222 nm. The data show that in Na_vAe1p introduction of neck region glycines increases the thermal liability of the measured transition following the rank order as expected from the crystal structures (Na_vAe1p > Na_vAe1p-3G > Na_vAe1p-7G) (Figure 3G). Notably, Na_vAe1p- Δ CTD lacks a cooperative thermal transition, demonstrating that the measured changes in thermal behavior arise from the CTD (Figure 3G). Further, Na_vSp1p is less stable than

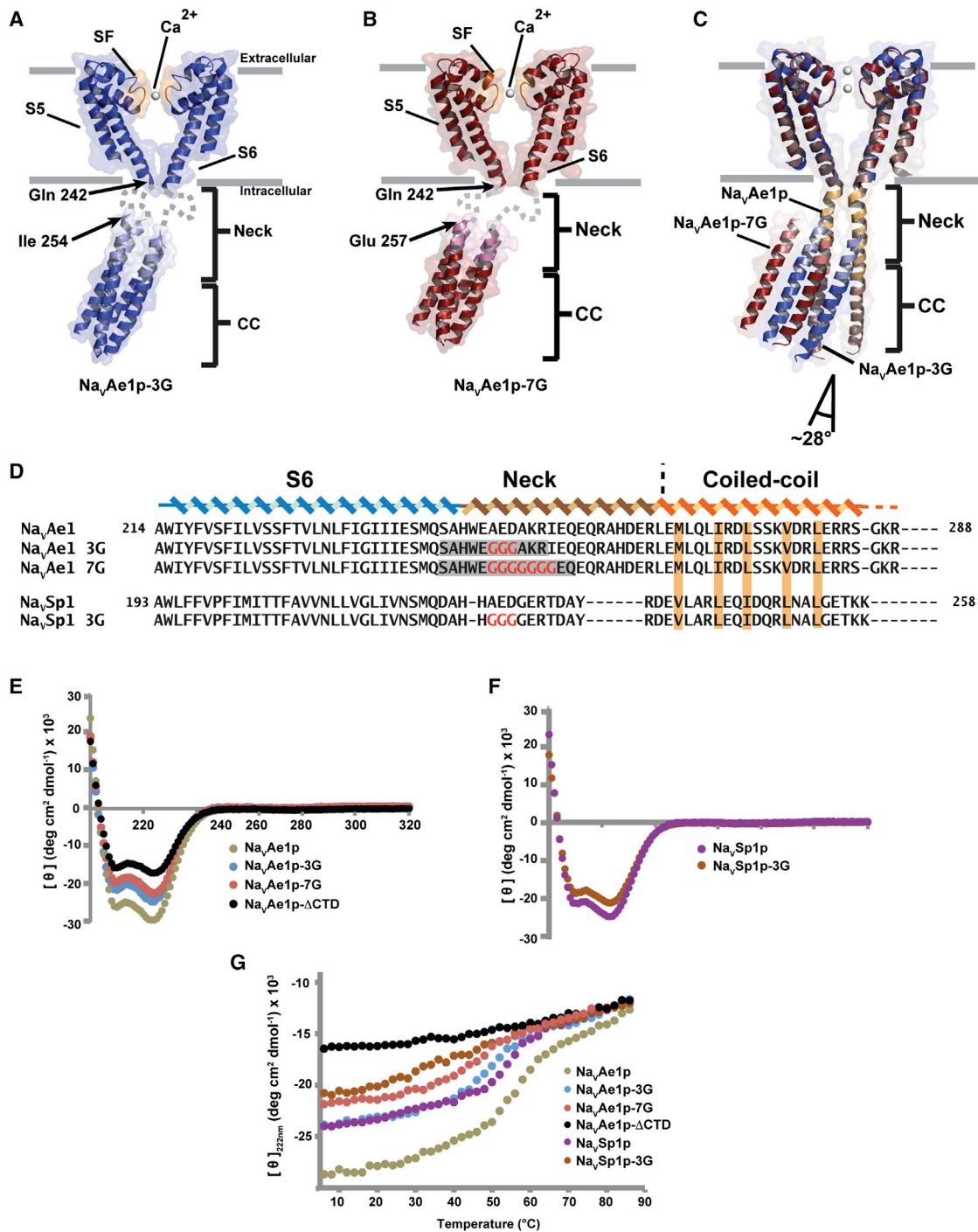


Figure 3. BacNa_v Neck Disruption Structural Outcomes

(A and B) Cartoons of two subunits of (A) Na_vAe1p-3G (dark blue) and (B) Na_vAe1p-7G (firebrick) structures. Grey dashes indicate regions lacking electron density. Residues defining the electron density limits are indicated. Selectivity filter is orange.

(C) Superposition of Na_vAe1p (orange) (Shaya et al., 2014), Na_vAe1p-3G (dark blue), and Na_vAe1p-7G (firebrick). Angle shows Na_vAe1p-7G coiled-coil displacement. Selectivity filter ion positions are shown.

(D) S6-CTD sequences for the indicated channels. Polyglycine positions are red. Regions lacking electron density are gray. Coiled-coil "a-d" repeat is orange.

(E and F) CD spectra for the indicated proteins at 4°C.

(G) Thermal denaturation curves for the indicated proteins.

See also Figures S3 and S4 and Table S3.

Na_vAe1p and the introduction of the triple glycine neck mutant in Na_vSp1p eliminated the thermal transition, in agreement with the function of the parent channels (Figures 1 and 2). Together, the crystallographic and CD data demonstrate that increasing BacNa_v neck flexibility leads to a loss of structure that is restricted to the neck, show that these changes increase the neck thermal sensitivity, and indicate that this disruption is the source of the functional changes caused by polyglycine substitution.

Electron Paramagnetic Resonance Spectroscopy Reveals Changes in Neck Dynamics

To investigate the CTD domain dynamics, we used site-specific spin labeling with the nitroxide spin probe (1-Oxyl-2,2,5,5-tetramethylpyrrolidine-3-methyl) methanethiosulfonate (MTSSL) and electron paramagnetic resonance (EPR) studies (Mchaourab et al., 2011). We probed select positions on the exterior of the Na_vAe1p and Na_vAe1p-3G CTDs by labeling three neck sites (Glu247 and Ala251 that frame polyglycine sites in Na_vAe1p-3G and Glu255 at the beginning of the Na_vAe1p-3G ordered region) (Figures 3A and 4A), three coiled-coil sites (Glu266, Gln269, and Asp273), and a site at the protein C terminus (Arg283) (Figure 4A). Double electron-electron resonance (DEER) spectroscopy indicated that, with the exception of Arg283, the probe positions in Na_vAe1p have spin echo decays with a well-defined oscillation (Figure 4B). The corresponding distance distributions match those expected from the structure (~25 Å and ~35 Å for adjacent and diagonal nitroxide positions, respectively). By contrast, introduction of triple glycine at residues 248–250 (Figure 4A) caused clear changes at Glu247 and Ala251. These decays showed evidence of superimposed longer component that is manifested in the distance distributions. We interpret this component as indicative of increased disorder (Figure 4B). Notably, minimal changes occurred at Glu255, in complete agreement with the order seen at this site in the crystal structure (Figure 3A). Further, no differences were observed at any coiled-coil positions. Thus, these data reinforce the view from our crystallographic studies that introduction of polyglycine sequences into the neck increase its mobility and spare the coiled-coil structure.

There are clear functional differences between Na_vAe1 and Na_vSp1 that originate in the CTD (Figure 1). Therefore, we probed Na_vSp1p at positions equivalent to those tested in Na_vAe1p and Na_vAe1p-3G (Figure S5) to see whether there was a structural correlate underlying the diverse functional properties. Na_vSp1p continuous wave (CW) and DEER studies reveal notable differences in the dynamics of the neck versus the coiled-coil. By contrast to Na_vAe1p, the Na_vSp1p neck positions consistently display DEER decays that have a longer distance component, similar to those in Na_vAe1p-3G, whereas the Na_vSp1p coiled-coiled DEER signals resemble what is observed in Na_vAe1p (Figure S5B). These differences between EPR probe mobility in the neck and coiled-coil is similar to those observed in Na_vMs (Bagn eris et al., 2013). Importantly, our data strongly support the notion from the chimera (Figure 2) and CD experiments (Figure 3G) that the neck domains of different BacNa_vs have diverse degrees of inherent order and that these differences are the origins of functional diversity.

Na_vAe1p Neck Has a Hydrophilic Core and a π -Stack Structure Important for Gating

In parallel with our studies of Na_vAe1p mutants, we obtained Na_vAe1p crystals that diffracted to superior resolution than previously reported (Shaya et al., 2014) (2.95Å versus 3.46Å, respectively) (Figures S6A and S6B; Table S3). Although the overall architecture is unchanged (Figure S6C), the increased resolution revealed previously uncharacterized CTD features. Notably, there is a striking bipartite organization in the core of the CTD neck and coiled-coil domains. The coiled-coil core follows the classic heptad repeat “a-d” packing (Lupas and Gruber, 2005) (Figures 5A–5C) and comprises five layers of hydrophobic residues (Met267, Ile271, Leu274, Val278, and Leu281) and a terminal, more open layer at Ser285 (Figures 5B and 5C). By contrast, the neck core is composed almost exclusively of hydrophilic side chains. These also follow a heptad pattern but include a one residue skip at the Gln256-Gln257 junction (Figure 5A). Consistent with the splaying of the neck helices (Shaya et al., 2014), the neck has a less well-packed core than the coiled-coil (Figures 5B and 5C). The stark differences between the structures and compositions of the neck and coiled-coil cores suggest that the neck is metastable and provide an explanation for why it is able to change structure during channel gating.

The 2.95 Å resolution Na_vAe1p structure revealed a number of interesting non-protein entities associated with the channel. There are two ions in the CTD core. One is at the N-terminal end of the neck, the “neck ion” (Shaya et al., 2014), and a second is at the neck/coiled-coil junction, the “coiled-coil ion” (Figure 5B). Data collected at the bromine absorption edge from Na_vAe1p crystals grown in 200 mM NaBr and soaked in cryoprotectant solutions containing 200 mM or 0 mM NaBr showed strong anomalous densities for both ions in 200 mM NaBr, but only for the coiled-coil ion in 0 mM NaBr (Figure S6D), demonstrating that both CTD ions are halogens and that the neck ion is labile. Based on these observations and the presence of chloride in the 2.95 Å structure crystallization conditions, we modeled both ions as chloride (Figure S6E). The selectivity filter has density corresponding to two sodium ions bridged by a water molecule. One sodium ion occupies the level of the Glu197 sidechain (corresponding to “site 2”) (Tang et al., 2014), and the second is found at the level of Thr195 (“site 3”) (Figure S6F). We also identified a number of lipids including one occupying a site observed in a number of other BacNa_v structures (Payandeh and Minor, 2015) that is located next to the P1 pore helix and wedged between the subunits (Figure S6G).

The neck ion binding site arises from an unusual motif, the “ π -stack,” in which Trp246 from one subunit makes a face-to-face stacking interaction with His245 from the neighbor (Figures 5B–5E) and creates a neck ion binding site coordinated by the Trp246 indole nitrogens. The coiled-coil ion binding site comprises successive “a-d-a” positions in the CTD core (Figures 5B, 5C, and 5F). Four guanido moieties from Arg264 that occupy the first ‘a’ position of the coiled-coil “a-d” repeat coordinate the halide ion (Figure 5F). This ionic complex forms an “electrostatic pin” in the helical bundle core. The Arg264 sidechains extend into the space that should be occupied by the preceding “d” side chains of the neck core. The presence of a small residue

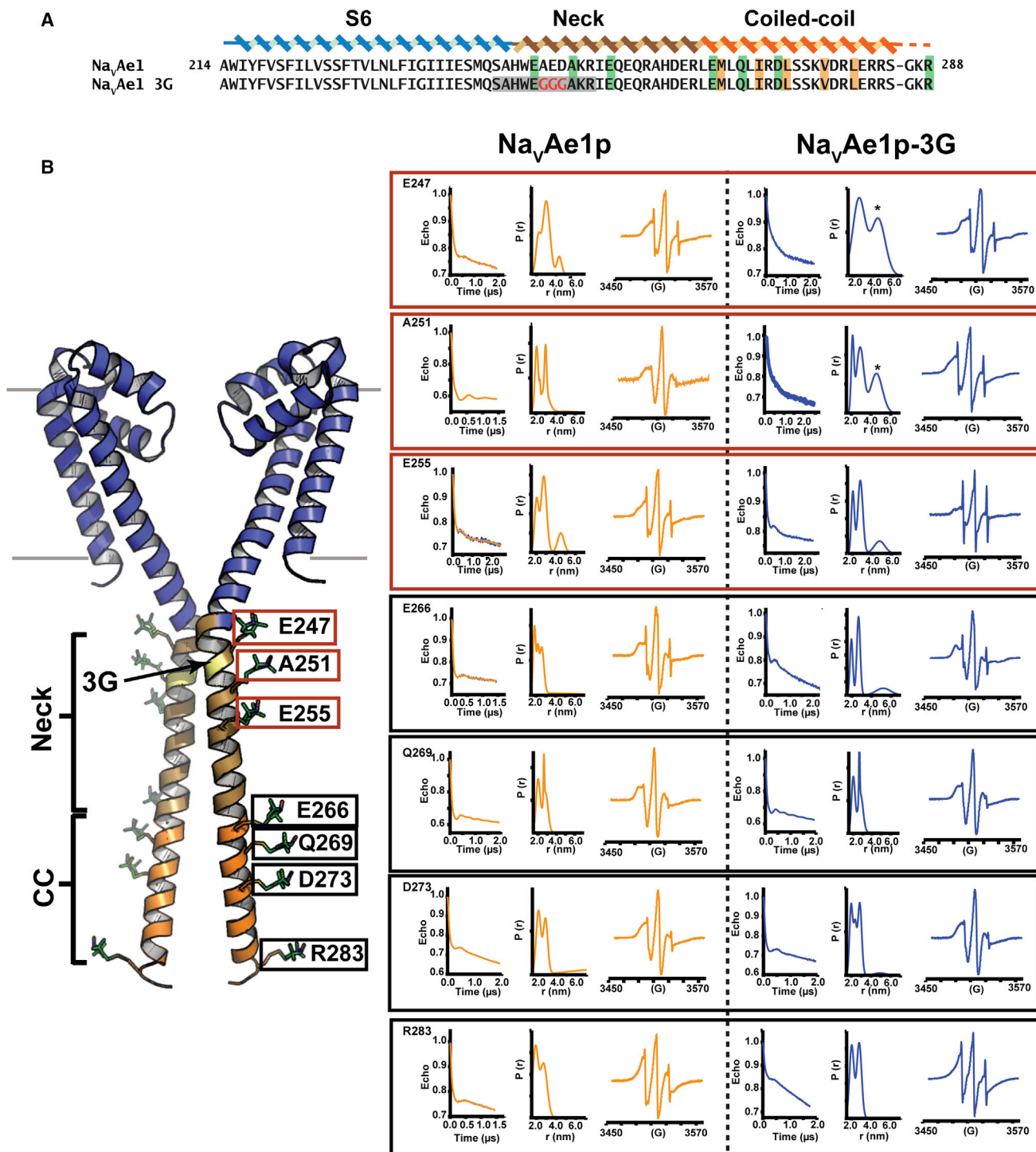


Figure 4. Na_vAe1p EPR Studies

(A) S6-CTD region sequences. Spin label positions, polyglycine substitutions and, Coiled-coil “a”-“d” repeat are highlighted green, red, and orange, respectively. Na_vAe1p-3G residues lacking electron density are gray.

(B) Na_vAe1p cartoon of two subunits and spin label sites. Pore domain, neck, and coiled-coil are slate, sand, and orange, respectively. Red and black boxes denote neck and coiled-coil spin-label positions, respectively. Panels show DEER decays, distance distributions, and CW spectra. Asterisks indicate the new Na_vAe1p-3G long-range distances.

See also [Figure S5](#).

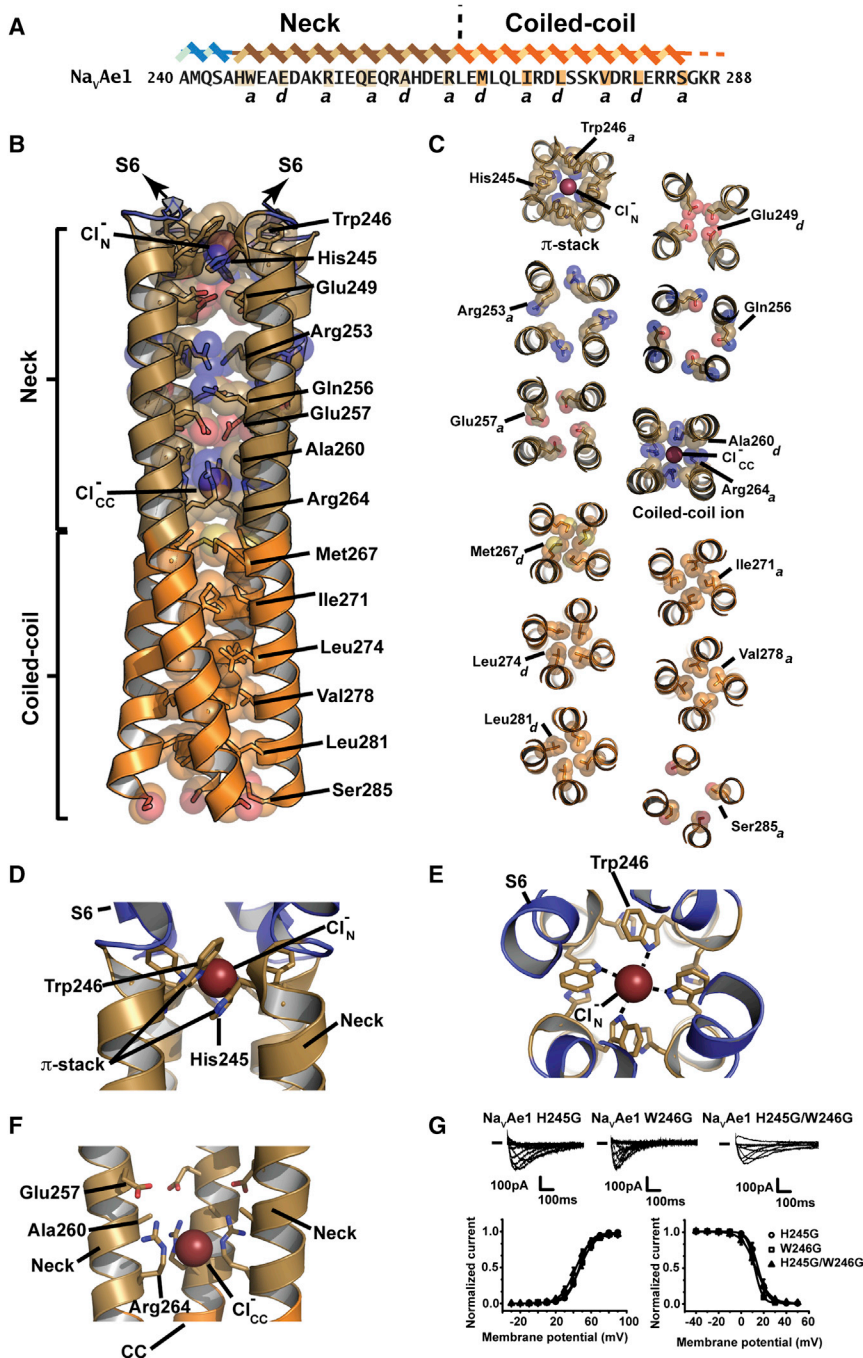


Figure 5. Na_vAe1p CTD Structure

(A) Na_vAe1 sequence. Neck and coiled-coil “a”-“d” core residues, His245, and Glu256 are highlighted.

(B) Na_vAe1p CTD cartoon showing core residues. Neck ion, Cl_N⁻, and Coiled-coil ion, Cl_{CC}⁻ are indicated. S6, neck, and coiled-coil are slate, sand, and orange, respectively.

(C) Na_vAe1p CTD π-stack, “a” and “d” layers, and Coiled-coil ion site packing geometries.

(D and E) π-stack ion binding site (D) side and (E) top views. His245, Trp246, and Neck ion, Cl_N⁻, are indicated.

(F) Coiled-coil ion binding site. Glu257, Ala260, Arg264, and coiled-coil ion, Cl_{CC}⁻ are indicated.

(G) Na_vAe1_{H245G}, Na_vAe1_{W246G}, and Na_vAe1_{H245G/W246G} exemplar currents and voltage-dependence of activation and inactivation. Colors are as in Figure 4.

See also Figures S6 and S7 and Table S3.

ing differences in the neck and coiled-coil ions and the metastable nature of the neck hydrophilic core versus the stable coiled-coil hydrophobic core. π-stack and coiled-coil ion motifs signatures occur in other BacNa_v sequences and indicate that these structures are present in other channels (Figure S7).

Because the Na_vAe1p-3G and Na_vAe1p-7G structures showed disrupted π-stack elements due to the polyglycine mutations (Figures 3A, 3B, 3D, and S6E), we wanted to test whether direct disruption of this structural element would affect function. As with other Na_vAe1 neck destabilizing mutations (Shaya et al., 2014), mutation of either π-stack residue to glycine resulted in measurable currents (Figure 5G). As expected from the intersubunit stacking, Na_vAe1_{H245G/W246G} had essentially identical voltage-dependent activation and inactivation properties compared to Na_vAe1_{H245G} and Na_vAe1_{W246G}, demonstrating that the two π-stack elements are co-dependent (Figure 5G; Table S1). A previous Na_vAe1_{H245G} low resolution structure showed that π-stack disruption leads to neck ion loss but little perturbation to the

at this position, Ala260, accommodates the Arg264 guanido moieties and permits them to interact with the Glu257 carboxylates from the “a” position above (Figures 5C and 5F). Interestingly, the “electrostatic pin” formed by the coiled-coil ion binding site marks where the CTD helices diverge from the canonical coiled-coil packing. Further, in the Na_vAe1p-3G and Na_vAe1p-7G structures, disruption of the helical structure propagates through the π-stack but stops at the coiled-coil ion binding site (Figure S6E). These observations agree with the apparent bind-

neck helix (Shaya et al., 2014). Thus, the π-stack architecture serves as a type of lock in the Na_vAe1 neck to oppose channel opening.

BacNa_v Neck Is Energetically Coupled to the Channel Gate

Does the BacNa_v neck affect function by impacting the channel gate, the voltage sensors, or both? To answer this question, we pursued a double mutant cycle strategy (DeCaen et al., 2009;

Yifrach and MacKinnon, 2002) examining whether disruption of the Na_vSp1 neck by the GGG substitution, Na_vSp1_{GGG}, had additive or non-additive effects on voltage gating when placed in the context of mutations that perturb the gate or the voltage sensors. To test whether the neck and gate are coupled, we compared the properties of the Na_vSp1 channel gate mutant, Na_vSp1_{M220A} (Shaya et al., 2014), Na_vSp1_{GGG}, and a channel bearing both mutations Na_vSp1_{M220A/GGG} (Figures 6A and 6B). To probe for coupling to the voltage sensors, we neutralized each of the four arginines at BacNa_v S4 voltage sensor positions R1–R4 (Payandeh et al., 2011; Zhang et al., 2012) by mutation to glutamine (Figure 6C) in order to perturb the ease of voltage sensor movement and measured the properties of Na_vSp1_{R1Q}, Na_vSp1_{R2Q}, Na_vSp1_{R3Q}, and Na_vSp1_{R4Q}, alone and in combination with the GGG neck mutation (Figures 6D and 6E).

As observed previously, gate destabilization, Na_vSp1_{M220A} (Shaya et al., 2014), and neck disruption, Na_vSp1_{GGG} (Shaya et al., 2014), caused substantial leftward shifts in the activation $V_{1/2}$ (27.7 ± 1.6 mV, -10.5 ± 2.1 mV, and -18.6 ± 2.7 mV for $V_{1/2}$ of Na_vSp1, Na_vSp1_{GGG}, and Na_vSp1_{M220A}, respectively) (Figure 6B; Table S4). Combining both, Na_vSp1_{M220A/GGG}, resulted in a $V_{1/2}$ left shift beyond that of the individual changes (-28.3 ± 4.0 mV) (Figure 6B; Table S4). R1 neutralization did not affect the activation $V_{1/2}$ (31.1 ± 1.2 mV), whereas other arginine position neutralizations shifted the activation $V_{1/2}$ in either the positive (Na_vSp1_{R2Q} and Na_vSp1_{R4Q}, 44.8 ± 2.1 mV and 59.9 ± 3.2 mV, respectively) or negative (Na_vSp1_{R3Q}, 11.7 ± 2.3 mV) directions relative to Na_vSp1 (Figure 6E; Table S4). In each case, combination with GGG neck mutation caused a substantial left shift in $V_{1/2}$ (Figure 6E) (Na_vSp1_{R1Q/GGG}, Na_vSp1_{R2Q/GGG}, Na_vSp1_{R3Q/GGG}, and Na_vSp1_{R4Q/GGG}, -9.2 ± 1.9 mV, 44.8 ± 2.1 mV, -24.5 ± 1.8 mV, and 32.7 ± 2.0 mV, respectively).

By taking changes in $V_{1/2}$, estimated gating charge, $Z(e_0)$, and slope factor (k) (DeCaen et al., 2009; Yifrach and MacKinnon, 2002), we determined the activation-free energy at 0 mV. Comparison of measured double mutant-free energy perturbations relative to Na_vSp1 ($\Delta\Delta G^{\circ}_{\text{obs}}$) with values calculated additive effects of individual mutants ($\Delta\Delta G^{\circ}_{\text{calc}}$) revealed a clear contrast between how neck perturbation affects the pore and voltage sensors (Table S4). $\Delta\Delta G^{\circ}_{\text{obs}}$ for the neck-gate combination, Na_vSp1_{M220A/GGG}, -3.1 kcal mol⁻¹, is substantially less than that expected from the individual changes ($\Delta\Delta G^{\circ}_{\text{calc}} = -5.0$ kcal mol⁻¹) (Table S4). By contrast, $\Delta\Delta G^{\circ}_{\text{obs}} = \Delta\Delta G^{\circ}_{\text{calc}}$ for all neck-voltage sensor pairs (Table S4). Thus, these data indicate that the neck affects gating voltage dependence by direct perturbation of the channel gate. Given its location and the importance of neck structure, such an effect must come from the ability of the neck to constrain pore opening.

DISCUSSION

VGIC cytosolic domains are important channel modulation loci. Hence, there is a great interest in understanding how their structural transformations affect VGIC transmembrane channel core. The simple BacNa_v CTD architecture, comprising four parallel helices, provides an elegant paradigm for defining how VGIC CTDs can influence channel gating. Our studies of BacNa_v CTDs reveal a VGIC modulation mechanism built on the bipartite

architecture of the BacNa_v CTD four-helix bundle. The key feature, the neck domain, is a membrane proximal four-helix bundle bearing a hydrophilic core that forms a metastable structure. This domain is constrained on its N and C termini by the channel pore domain and a classic parallel four-stranded coiled-coil, respectively. These physical constraints are essential for the neck to influence voltage-dependent gating and their importance is supported by two key observations: (1) deletions of the entire CTD (Figures 1G and 1H; Table S1) shift the voltage-dependent gating in the hyperpolarized direction in a manner equivalent to deletion of only the coiled-coil (Figure 1; Table S1), and (2) mutant cycle analysis shows strong energetic coupling between the activation gate of the channel pore and the neck (Figure 6; Table S4).

The origin of the wide range of BacNa_v voltage-dependent activation responses has been unclear (Scheuer, 2014). The diverse and largely hydrophilic nature of BacNa_v neck domains contrasts with the well-conserved CTD coiled-coil and high conservation of key voltage sensor domain elements (Payandeh and Minor, 2015). This neck sequence diversity, together with the capacity of different BacNa_v CTDs to tune voltage-responses of the Na_vSp1 transmembrane core by >65 mV (Figures 2A–2C), indicates that even though features of the transmembrane domains are likely to set some voltage-depending gating properties, much of the varied voltage responses among BacNa_vs arises from differences in neck domain properties. These gating effects are directly correlated with the ability of the neck to adopt a stable structure. Studies of chimeras containing the Na_vSp1 transmembrane domain and CTDs from other BacNa_vs show that channels having the Na_vBh1 neck, which is disordered (Powl et al., 2010), have a voltage sensitivity that is equivalent to those lacking the entire CTD (Figures 1H and 2C), whereas those having a completely ordered CTD, Na_vAe1 (Shaya et al., 2014), require stronger depolarizations to open. Further, structural and functional studies show that increased neck disorder shifts the activation of both Na_vAe1 and Na_vSp1 to more hyperpolarized potentials (Figure 3) (Shaya et al., 2014). In this regard, our discovery of the “ π -stack” halogen-binding site (Figures 5D and 5E) provides a clear explanation for why Na_vAe1, among all other BacNa_vs, can only be opened if the neck is destabilized.

Previous deletion studies of different BacNa_vs reported varied effects, including a left shift in voltage-dependent activation for Na_vSuP1 (Irie et al., 2012) and no change for Na_vBh1 (Mio et al., 2010), and provided no clear view of why there were different outcomes in different channel contexts. Our data now point to a unified mechanism for BacNa_v gating in which the CTDs tune the ease of voltage-dependent opening of the channel based on the propensity of the neck region to adopt an ordered state. Due to its high polar residue content, the neck structure is metastable and contrasts with the stable hydrophobic core of the terminal coiled coil. This property is critical for the neck to undergo the order \rightarrow disorder transition associated with channel opening (Figure 7A). Although CTD mutations can impact channel inactivation properties (Figures S1B–S1D) (Bagneris et al., 2013; Irie et al., 2010, 2012; Tsai et al., 2013), the effects are diverse in different BacNa_vs and likely reflect a complex inactivation process that also involves key contributions from elements of the pore domain (Pavlov et al., 2005; Payandeh et al.,

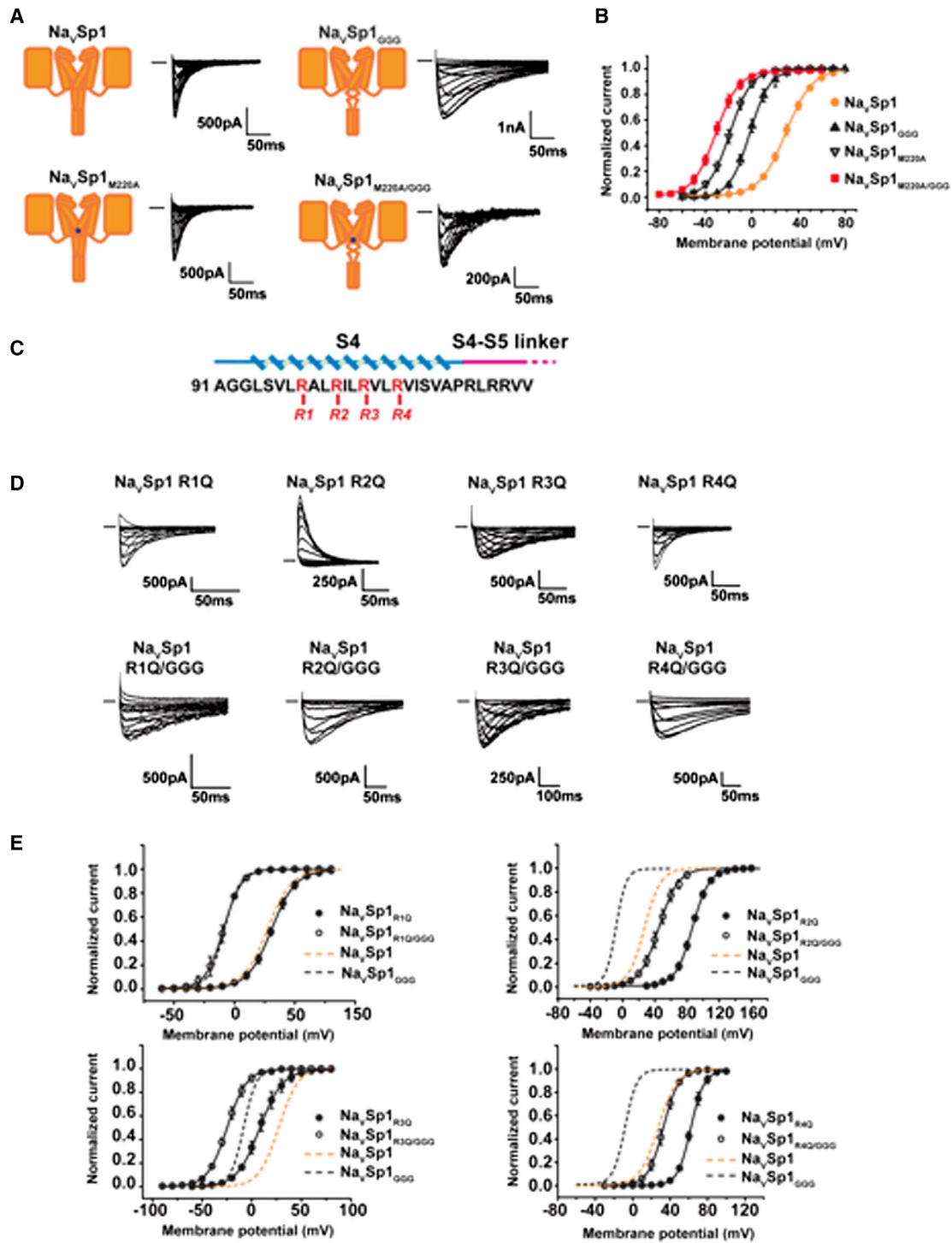


Figure 6. BacNa_v CTD Couples to the Intracellular Gate

(A) Na_vSp1, Na_vSp1_{GGG}, Na_vSp1_{M220A}, and Na_vSp1_{M220A/GGG} exemplar currents.

(B) Activation curves from (A).

(C) Na_vSp1 S4 mutant sites.

(D) Na_vSp1 R1-R4 and R1-R4/GGG mutant exemplar currents.

(E) Voltage-dependent activation curves for the indicated mutants. Na_vSp1 (tan dashes) and Na_vSp1_{GGG} (black dashes) curves are shown for reference.

See also Table S4.

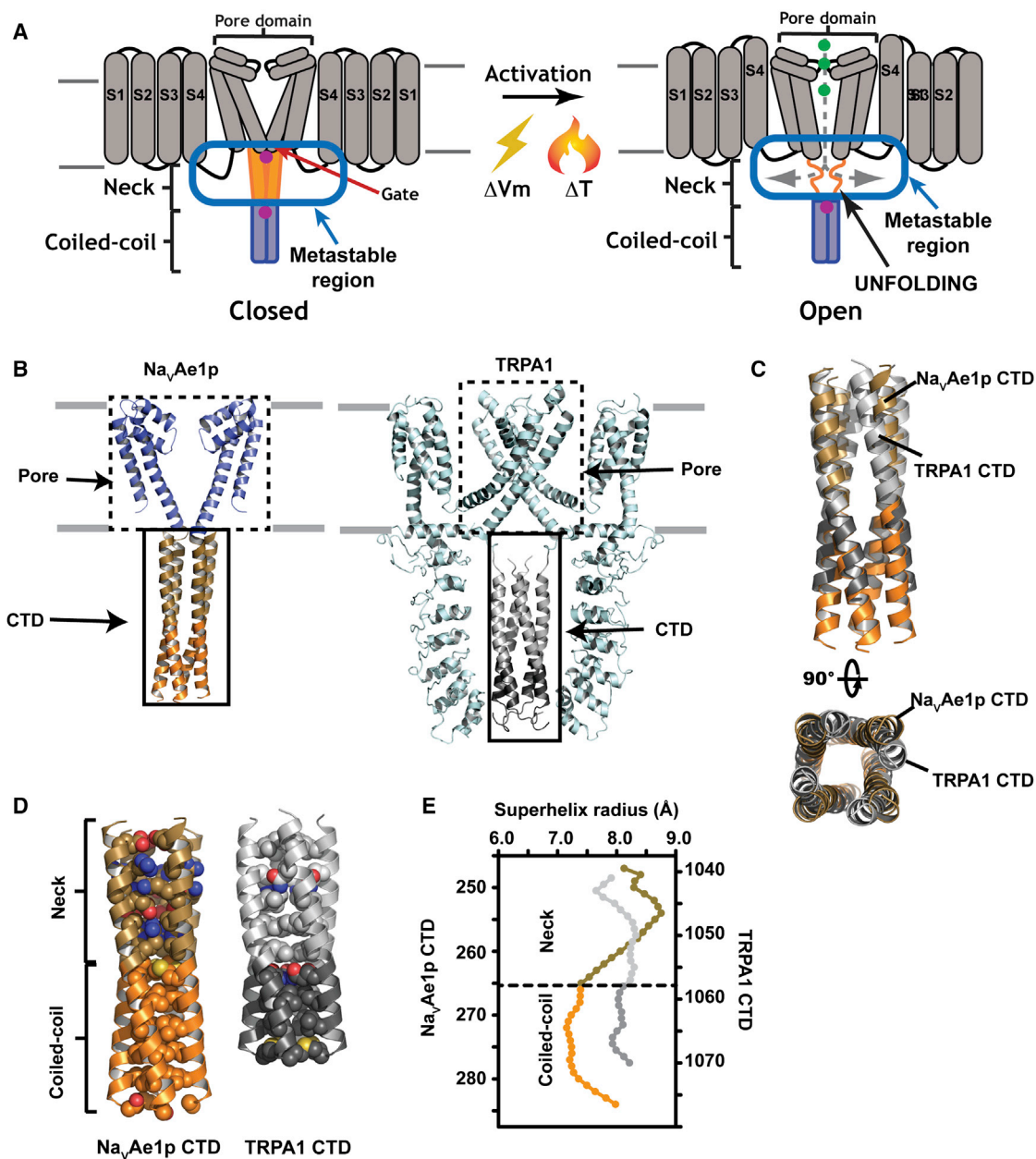


Figure 7. Function and Structural Conservation of VGIC Superfamily CTD Four-Helix Bundles

(A) BacNa_v gating is coupled to a neck unfolding transition. Purple circles indicate neck and coiled-coil ions. (B) Na_vAe1p (left) and TRPA1 (Paulsen et al., 2015) (right) cartoon diagrams CTD four-helix bundle is indicated. (C) Na_vAe1p and TRPA1 coiled-coil superposition. TRPA1 shading indicates regions corresponding to the Na_vAe1p neck (light gray) and coiled-coil (dark gray). (D) Comparison of Na_vAe1p (left) and TRPA1 (right) CTD cores. TRPA1 CTD-buried hydrophilic residues are Gln1047 and Gln1061. (E) Na_vAe1p and TRPA1 CTD superhelix radii comparison. Colors are as in (C). See also Table S5.

2012; Shaya et al., 2014). Thus, the clear systemic effects we observe here regarding how neck structure affects activation leads us to propose a gating mechanism in which the order of the neck is directly linked to the ease of channel opening.

Our studies revealed two ion binding sites that contribute to CTD functional properties and neck rigidity. The Na_vAe1

“π-stack” motif is found in other halophile BacNa_vs (Figure S7) and may serve as a point of ion-mediated modulation. The coiled-coil ion binding site comprises an E/Q/D/N/A-A-R motif at successive “a”-“d”-“a” positions and is more prevalent among BacNa_vs (Figure S7). This structure forms the lower boundary of loss of structure in neck disruptions (Figures 3A,

3B, and S6E) and provides a structural transition between the hydrophobic core of the coiled-coil and more open, hydrophilic core of the neck. The modular nature of the BacNav CTD and relatively simple four-helix architecture points toward means to rationally engineer channel responses by controlling the stability of the neck domain using either chimeric approaches or by exploiting stabilizing motifs such as the π -stack.

Some VGIC superfamily members, such as TRPs (Brauchi et al., 2006; Clapham and Miller, 2011; Grandl et al., 2008; Vriens et al., 2014) and K_{2PS} (Bagriantsev et al., 2012; Lolicato et al., 2014; Maingret et al., 2000; Schneider et al., 2014) are gated by temperature. Whether ion channel temperature-dependent responses originate from the action of a single domain (Bagriantsev et al., 2012; Brauchi et al., 2006; Grandl et al., 2008) or a more distributed property (Chowdhury et al., 2014; Clapham and Miller, 2011; Vriens et al., 2014) remains under intense investigation. The NavSp1 activation $V_{1/2}$ has a strong temperature dependence (~ 35 mV over an $\sim 17^\circ\text{C}$ range) that is eliminated by increasing neck disorder (Figures 2D and 2E). Further, NavSp1 CTD chimeras having a similar, NavSp1_{PzCTD}, or more right shifted, NavSp1_{Ab1CTD}, $V_{1/2}$ responses also show a strong temperature dependence, suggesting that the activation threshold position coincides with a more structured neck. These acute temperature responses contrast with the <5 mV response of the Shaker voltage-gated potassium channel over a similar temperature range (Chowdhury et al., 2014). Although distributed elements may influence BacNav temperature responses (DeCaen et al., 2014), particularly in NavBh1 (NaChBac), which has a disordered CTD (Powl et al., 2010), our data demonstrate that it is possible for a single domain, the BacNav CTD neck, to control the temperature-dependent responses of a VGIC (Figures 2D and 2E). This result provides a definitive example of a defined temperature-sensing domain.

Structural studies of BacNavs (Shaya et al., 2014), KCNQ channels (Howard et al., 2007; Wiener et al., 2008), and TRP channels (Paulsen et al., 2015; Yu et al., 2012) establish the commonality of parallel four-stranded coiled-coil domains in the VGIC superfamily. Comparison of the NavAe1p and TRPA1 CTDs reveals striking similarity well beyond their shared location (Figures 7B and 7C). Superposition shows a close correspondence in the coiled-coil (Figures 7C and 7D; Table S5) and highlights NavAe1p neck helix splaying (Figure 7E). The more uniform TRPA1 coiled-coil has two layers of buried hydrophilic residues: an N-terminal one that matches the position of the NavAe1p neck and a second one corresponding to the neck:coiled-coil junction (Figures 7C and 7D). Buried hydrophilic residues in coiled-coil cores carry a well-established energetic penalty with respect to quaternary architecture stability (Lupas and Gruber, 2005). Although TRPA1 ankyrin repeats have been implicated in temperature responses (Cordero-Morales et al., 2011; Jabba et al., 2014), it is striking that they form a cage around the CTD (Figure 7B). Hence, many of the reported ankyrin repeat domain effects may be due to modulation of CTD transitions. It is also notable that the voltage-sensor only channel Hv1 has a similar temperature-sensitive membrane proximal coiled-coil domain bearing a buried polar residue in the region implicated in temperature responses (Fujiwara et al., 2012; Takeshita et al., 2014). Thus, the presence of buried polar residues in helical bundle do-

ains in distantly related VGIC superfamily members together with the demonstration that such a metastable domain can play a crucial role in controlling channel function suggests that the mechanism we describe for the BacNav CTD may occur in many VGIC superfamily members.

Control of ion channel function by physical and chemical cues is essential for producing dynamic changes in excitability (Hille, 2001). While the coupling between the voltage sensor and pore domains has been studied extensively (Lu et al., 2002; Payandeh et al., 2012; Yifrach and MacKinnon, 2002), mechanisms for how cytoplasmic domains modulate the pore remain imperfectly understood. The four-helix bundle architecture of the BacNav CTD provides a simple means to control channel gating. The metastable, but ordered, neck structure directly couples to the energetics of pore opening (Figure 6). This effect does not depend on voltage-sensor movement and likely affects a late step of channel activation. These observations support the idea that conformational changes in such structures can restrain and shape the energetics of channel pore opening (Shaya et al., 2014; Uysal et al., 2009). Consequently, helical bundle domains that bear buried polar residues proximal to a VGIC pore can provide a general mechanism for controlling the action of channels gated by different types of stimuli.

EXPERIMENTAL PROCEDURES

Construct Design and Cloning

NavSp1 (*Silicibacter pomeroyi*), NavAe1 (*Alkallimnicola ehrlichii*), chimeras, and mutants were cloned into pIRES2-EGFP vector (Clontech) (Shaya et al., 2014). Chimeric constructs were generated by PCR. Construct boundaries are found in the Supplemental Experimental Procedures. Mutants were made using QuikChange (Stratagene). All constructs were verified by complete DNA sequencing.

Patch-Clamp Electrophysiology

Overexpression and patch-clamp recording from NavSp1, NavAe1, mutants, and chimeras were performed as described (Shaya et al., 2014). Voltage dependence was analyzed with the Boltzmann equation, $y = 1/(1 + \exp[(V - V_{1/2})/s])$, where y is fractional activation, V is voltage, $V_{1/2}$ half-activation voltage, and s is the inverse slope factor (mV). Details are found in the Supplemental Experimental Procedures.

Surface Biotinylation Assay

Surface expression was measured in HEK293 cells plated for each HA-tagged construct at 4°C . Samples were analyzed on SDS-PAGE and western blot detected. Details are found in the Supplemental Experimental Procedures.

Protein Purification and Crystallization

NavAe1p was expressed and purified as described previously (Shaya et al., 2011, 2014) except that for the size exclusion chromatography step the running buffer included 150 mM NaCl, 50 mM CaCl₂, 0.3 mM β -dodecyl maltoside (DDM), 20 mM Na-HEPES, pH (8.0). Constructs for NavAe1p-3G and NavAe1p-7G were expressed in *Escherichia coli* (DE3) C41 (Miroux and Walker, 1996) using a previously described NavAe1p vector (Shaya et al., 2011). Details of expression, purification, and preparation of selenomethionine-labeled NavAe1p-3G are found in the Supplemental Experimental Procedures.

Crystallization and Structure Determination

NavAe1p crystals were grown by hanging drop vapor diffusion. NavAe1p-3G, NavAe1p-3G SeMet, and NavAe1p-7G crystals were grown by microbatch under oil. NavAe1p, NavAe1p-NaBr complexes, and NavAe1p-3G SeMet diffraction data were collected at Advanced Photon Source Beamline 23ID-B, Argonne National Laboratory. NavAe1p-3G and NavAe1p-7G diffraction data

were collected at Advanced Light Source Beamline 8.3.1, Lawrence Berkeley National Laboratory. Details for crystallization, data collection, structure determination, and model refinement can be found in the [Supplemental Experimental Procedures](#).

Circular Dichroism Spectroscopy

CD spectra were recorded on an Aviv 215 spectrometer in a 1 mm pathlength quartz cell at 4°C. BacNa_v pore domains were purified as above, exchanged into 10 mM sodium phosphate pH (7.4), 100 mM NaCl, 0.3 mM β-DDM, and concentrated to ~24–26 μM. Wavelength scans were recorded in triplicate from 190 to 320 nm with a 1 nm step size averaged over 10 s. Thermal melts were as described (Shaya et al., 2011).

EPR Labeling and Sample Preparation

Single cysteine mutants of Na_vAe1p, Na_vAe1p-3G, and Na_vSp1p were generated by quick-change mutagenesis and were purified as above using 1 mM TCEP in all buffers and labeled with MTSSL. CW-spectra were collected on a Bruker EMX at 10 mW power with a modulation amplitude of 1.6G. All spectra were normalized to the double integral. DEER experiments were carried out using a standard four-pulse protocol (Jeschke, 2002). Details can be found in the [Supplemental Experimental Procedures](#).

ACCESSION NUMBERS

The accession numbers for the Coordinates and structure factors reported in this paper are RCSB PDB: 5HJ8, 5HK6, 5HKD, 5HK7, 5HKT, and 5HKU.

SUPPLEMENTAL INFORMATION

Supplemental Information includes Supplemental Experimental Procedures, seven figures, and five tables and can be found with this article online at <http://dx.doi.org/10.1016/j.cell.2016.02.001>.

AUTHOR CONTRIBUTIONS

C.A., A.R., and D.L.M. conceived the study and designed the experiments. C.A., A.R., D.S., F.F., R.A.S., S.R.N., and S.M. performed the experiments. C.A. performed electrophysiological experiments and analyzed the data. A.R., D.S., and S.R.N. purified the proteins. A.R. crystallized and determined the structures of polyglycine mutants, performed the CD experiments, prepared EPR samples, and analyzed the data. D.S. grew the Na_vAe1p crystals, collected the data, and solved the structure. F.F. solved and refined the structures and analyzed the data. A.R., S.M., and S.A.R. prepared the EPR samples. S.M. and S.A.R. collected the EPR data. H.S.M. supervised the EPR experiments. A.R., R.A.S., H.S.M., and D.L.M. analyzed the EPR data. D.L.M. analyzed the data and provided guidance and support throughout. C.A., A.R., D.S., F.F., R.A.S., H.S.M., and D.L.M. wrote the paper.

ACKNOWLEDGMENTS

We thank M. Grabe, L. Jan, A. Moroni, and the D.L.M. lab members for manuscript comments. This work was supported by grants U54 GM087519 to H.S.M., R01-HL080050, R01-DC007664, and U54-GM094625 to D.L.M., and to C.A. from the American Heart Association. C.A. is an AHA postdoctoral fellow.

Received: August 7, 2015

Revised: December 22, 2015

Accepted: January 28, 2016

Published: February 25, 2016

REFERENCES

Bagn ris, C., DeCaen, P.G., Hall, B.A., Naylor, C.E., Clapham, D.E., Kay, C.W., and Wallace, B.A. (2013). Role of the C-terminal domain in the structure and function of tetrameric sodium channels. *Nat. Commun.* 4, 2465.

Bagriantsev, S.N., Clark, K.A., and Minor, D.L., Jr. (2012). Metabolic and thermal stimuli control K(2P)2.1 (TREK-1) through modular sensory and gating domains. *EMBO J.* 31, 3297–3308.

Berova, N., Nakanishi, K., and Woody, R.W. (2000). *Circular Dichroism: Principles and Applications*, Second Edition (Wiley-VCH).

Brauchi, S., Orta, G., Salazar, M., Rosenmann, E., and Latorre, R. (2006). A hot-sensing cold receptor: C-terminal domain determines thermosensation in transient receptor potential channels. *J. Neurosci.* 26, 4835–4840.

Chowdhury, S., Jarecki, B.W., and Chanda, B. (2014). A molecular framework for temperature-dependent gating of ion channels. *Cell* 158, 1148–1158.

Clapham, D.E., and Miller, C. (2011). A thermodynamic framework for understanding temperature sensing by transient receptor potential (TRP) channels. *Proc. Natl. Acad. Sci. USA* 108, 19492–19497.

Cordero-Morales, J.F., Gracheva, E.O., and Julius, D. (2011). Cytoplasmic ankyrin repeats of transient receptor potential A1 (TRPA1) dictate sensitivity to thermal and chemical stimuli. *Proc. Natl. Acad. Sci. USA* 108, E1184–E1191.

DeCaen, P.G., Yarov-Yarovoy, V., Sharp, E.M., Scheuer, T., and Catterall, W.A. (2009). Sequential formation of ion pairs during activation of a sodium channel voltage sensor. *Proc. Natl. Acad. Sci. USA* 106, 22498–22503.

DeCaen, P.G., Takahashi, Y., Krulwich, T.A., Ito, M., and Clapham, D.E. (2014). Ionic selectivity and thermal adaptations within the voltage-gated sodium channel family of alkaliphilic *Bacillus*. *eLife* 3.

Fujiwara, Y., Kurokawa, T., Takeshita, K., Kobayashi, M., Okochi, Y., Nakagawa, A., and Okamura, Y. (2012). The cytoplasmic coiled-coil mediates cooperative gating temperature sensitivity in the voltage-gated H(+) channel Hv1. *Nat. Commun.* 3, 816.

Grandl, J., Hu, H., Bandell, M., Bursulaya, B., Schmidt, M., Petrus, M., and Patapoutian, A. (2008). Pore region of TRPV3 ion channel is specifically required for heat activation. *Nat. Neurosci.* 11, 1007–1013.

Hille, B. (2001). *Ion Channels of Excitable Membranes*, Third Edition (Sinauer Associates, Inc.).

Howard, R.J., Clark, K.A., Holton, J.M., and Minor, D.L., Jr. (2007). Structural insight into KCNQ (Kv7) channel assembly and channelopathy. *Neuron* 53, 663–675.

Irie, K., Kitagawa, K., Nagura, H., Imai, T., Shimomura, T., and Fujiyoshi, Y. (2010). Comparative study of the gating motif and C-type inactivation in prokaryotic voltage-gated sodium channels. *J. Biol. Chem.* 285, 3685–3694.

Irie, K., Shimomura, T., and Fujiyoshi, Y. (2012). The C-terminal helical bundle of the tetrameric prokaryotic sodium channel accelerates the inactivation rate. *Nat. Commun.* 3, 793.

Jabba, S., Goyal, R., Sosa-Pag n, J.O., Moldenhauer, H., Wu, J., Kalmeta, B., Bandell, M., Latorre, R., Patapoutian, A., and Grandl, J. (2014). Directionality of temperature activation in mouse TRPA1 ion channel can be inverted by single-point mutations in ankyrin repeat six. *Neuron* 82, 1017–1031.

Jeschke, G. (2002). Distance measurements in the nanometer range by pulse EPR. *Chemphyschem* 3, 927–932.

Jiang, Y., Lee, A., Chen, J., Cadene, M., Chait, B.T., and MacKinnon, R. (2002). Crystal structure and mechanism of a calcium-gated potassium channel. *Nature* 417, 515–522.

Koishi, R., Xu, H., Ren, D., Navarro, B., Spiller, B.W., Shi, Q., and Clapham, D.E. (2004). A superfamily of voltage-gated sodium channels in bacteria. *J. Biol. Chem.* 279, 9532–9538.

Lolicato, M., Riegelhaupt, P.M., Arrigoni, C., Clark, K.A., and Minor, D.L., Jr. (2014). Transmembrane helix straightening and buckling underlies activation of mechanosensitive and thermosensitive K(2P) channels. *Neuron* 84, 1198–1212.

Lu, Z., Klem, A.M., and Ramu, Y. (2002). Coupling between voltage sensors and activation gate in voltage-gated K⁺ channels. *J. Gen. Physiol.* 120, 663–676.

Lupas, A.N., and Gruber, M. (2005). The structure of α-helical coiled coils. *Adv. Protein Chem.* 70, 37–78.

- Maingret, F., Lauritzen, I., Patel, A.J., Heurteaux, C., Reyes, R., Lesage, F., Lazdunski, M., and Honoré, E. (2000). TREK-1 is a heat-activated background K(+) channel. *EMBO J.* *19*, 2483–2491.
- McCusker, E.C., Bagnéris, C., Naylor, C.E., Cole, A.R., D'Avanzo, N., Nichols, C.G., and Wallace, B.A. (2012). Structure of a bacterial voltage-gated sodium channel pore reveals mechanisms of opening and closing. *Nat. Commun.* *3*, 1102.
- Mchaourab, H.S., Steed, P.R., and Kazmier, K. (2011). Toward the fourth dimension of membrane protein structure: insight into dynamics from spin-labeling EPR spectroscopy. *Structure* *19*, 1549–1561.
- Mio, K., Mio, M., Arisaka, F., Sato, M., and Sato, C. (2010). The C-terminal coiled-coil of the bacterial voltage-gated sodium channel NaChBac is not essential for tetramer formation, but stabilizes subunit-to-subunit interactions. *Prog. Biophys. Mol. Biol.* *103*, 111–121.
- Miroux, B., and Walker, J.E. (1996). Over-production of proteins in *Escherichia coli*: mutant hosts that allow synthesis of some membrane proteins and globular proteins at high levels. *J. Mol. Biol.* *260*, 289–298.
- Morais-Cabral, J.H., and Robertson, G.A. (2015). The enigmatic cytoplasmic regions of KCNH channels. *J. Mol. Biol.* *427*, 67–76.
- Paulsen, C.E., Armache, J.P., Gao, Y., Cheng, Y., and Julius, D. (2015). Structure of the TRPA1 ion channel suggests regulatory mechanisms. *Nature* *520*, 511–517.
- Pavlov, E., Bladen, C., Winkfein, R., Diao, C., Dhaliwal, P., and French, R.J. (2005). The pore, not cytoplasmic domains, underlies inactivation in a prokaryotic sodium channel. *Biophys. J.* *89*, 232–242.
- Payandeh, J., and Minor, D.L., Jr. (2015). Bacterial voltage-gated sodium channels (BacNa(Vs)) from the soil, sea, and salt lakes enlighten molecular mechanisms of electrical signaling and pharmacology in the brain and heart. *J. Mol. Biol.* *427*, 3–30.
- Payandeh, J., Scheuer, T., Zheng, N., and Catterall, W.A. (2011). The crystal structure of a voltage-gated sodium channel. *Nature* *475*, 353–358.
- Payandeh, J., Gamal El-Din, T.M., Scheuer, T., Zheng, N., and Catterall, W.A. (2012). Crystal structure of a voltage-gated sodium channel in two potentially inactivated states. *Nature* *486*, 135–139.
- Pioletti, M., Findeisen, F., Hura, G.L., and Minor, D.L., Jr. (2006). Three-dimensional structure of the KChIP1-Kv4.3 T1 complex reveals a cross-shaped octamer. *Nat. Struct. Mol. Biol.* *13*, 987–995.
- Powl, A.M., O'Reilly, A.O., Miles, A.J., and Wallace, B.A. (2010). Synchrotron radiation circular dichroism spectroscopy-defined structure of the C-terminal domain of NaChBac and its role in channel assembly. *Proc. Natl. Acad. Sci. USA* *107*, 14064–14069.
- Ren, D., Navarro, B., Xu, H., Yue, L., Shi, Q., and Clapham, D.E. (2001). A prokaryotic voltage-gated sodium channel. *Science* *294*, 2372–2375.
- Scheuer, T. (2014). Bacterial sodium channels: models for eukaryotic sodium and calcium channels. *Handbook Exp. Pharmacol.* *227*, 269–291.
- Schneider, E.R., Anderson, E.O., Gracheva, E.O., and Bagriantsev, S.N. (2014). Temperature sensitivity of two-pore (K2P) potassium channels. *Curr. Top. Membr.* *74*, 113–133.
- Shaya, D., Kreir, M., Robbins, R.A., Wong, S., Hammon, J., Brüggemann, A., and Minor, D.L., Jr. (2011). Voltage-gated sodium channel (NaV) protein dissection creates a set of functional pore-only proteins. *Proc. Natl. Acad. Sci. USA* *108*, 12313–12318.
- Shaya, D., Findeisen, F., Abderemane-Ali, F., Arrigoni, C., Wong, S., Nurva, S.R., Loussouarn, G., and Minor, D.L., Jr. (2014). Structure of a prokaryotic sodium channel pore reveals essential gating elements and an outer ion binding site common to eukaryotic channels. *J. Mol. Biol.* *426*, 467–483.
- Takeshita, K., Sakata, S., Yamashita, E., Fujiwara, Y., Kawanabe, A., Kurokawa, T., Okochi, Y., Matsuda, M., Narita, H., Okamura, Y., and Nakagawa, A. (2014). X-ray crystal structure of voltage-gated proton channel. *Nat. Struct. Mol. Biol.* *21*, 352–357.
- Tang, L., Gamal El-Din, T.M., Payandeh, J., Martinez, G.Q., Heard, T.M., Scheuer, T., Zheng, N., and Catterall, W.A. (2014). Structural basis for Ca²⁺ selectivity of a voltage-gated calcium channel. *Nature* *505*, 56–61.
- Tsai, C.J., Tani, K., Irie, K., Hiroaki, Y., Shimomura, T., McMillan, D.G., Cook, G.M., Schertler, G.F., Fujiyoshi, Y., and Li, X.D. (2013). Two alternative conformations of a voltage-gated sodium channel. *J. Mol. Biol.* *425*, 4074–4088.
- Ulmschneider, M.B., Bagnéris, C., McCusker, E.C., DeCaen, P.G., Delling, M., Clapham, D.E., Ulmschneider, J.P., and Wallace, B.A. (2013). Molecular dynamics of ion transport through the open conformation of a bacterial voltage-gated sodium channel. *Proc. Natl. Acad. Sci. USA* *110*, 6364–6369.
- Uysal, S., Vásquez, V., Tereshko, V., Esaki, K., Fellouse, F.A., Sidhu, S.S., Koide, S., Perozo, E., and Kossiakoff, A. (2009). Crystal structure of full-length KcsA in its closed conformation. *Proc. Natl. Acad. Sci. USA* *106*, 6644–6649.
- Vargas, E., Yarov-Yarovoy, V., Khalili-Araghi, F., Catterall, W.A., Klein, M.L., Tarek, M., Lindahl, E., Schulten, K., Perozo, E., Bezanilla, F., and Roux, B. (2012). An emerging consensus on voltage-dependent gating from computational modeling and molecular dynamics simulations. *J. Gen. Physiol.* *140*, 587–594.
- Vriens, J., Nilius, B., and Voets, T. (2014). Peripheral thermosensation in mammals. *Nat. Rev. Neurosci.* *15*, 573–589.
- Wiener, R., Haitin, Y., Shamgar, L., Fernández-Alonso, M.C., Martos, A., Chomsky-Hecht, O., Rivas, G., Attali, B., and Hirsch, J.A. (2008). The KCNQ1 (Kv7.1) COOH terminus, a multitiered scaffold for subunit assembly and protein interaction. *J. Biol. Chem.* *283*, 5815–5830.
- Yang, H., Zhang, G., and Cui, J. (2015). BK channels: multiple sensors, one activation gate. *Front. Physiol.* *6*, 29.
- Yifrach, O., and MacKinnon, R. (2002). Energetics of pore opening in a voltage-gated K(+) channel. *Cell* *111*, 231–239.
- Yu, F.H., Yarov-Yarovoy, V., Gutman, G.A., and Catterall, W.A. (2005). Overview of molecular relationships in the voltage-gated ion channel superfamily. *Pharmacol. Rev.* *57*, 387–395.
- Yu, Y., Ulbrich, M.H., Li, M.H., Dobbins, S., Zhang, W.K., Tong, L., Isacoff, E.Y., and Yang, J. (2012). Molecular mechanism of the assembly of an acid-sensing receptor ion channel complex. *Nat. Commun.* *3*, 1252.
- Yuan, P., Leonetti, M.D., Pico, A.R., Hsiung, Y., and MacKinnon, R. (2010). Structure of the human BK channel Ca²⁺-activation apparatus at 3.0 Å resolution. *Science* *329*, 182–186.
- Zagotta, W.N., Olivier, N.B., Black, K.D., Young, E.C., Olson, R., and Gouaux, E. (2003). Structural basis for modulation and agonist specificity of HCN pacemaker channels. *Nature* *425*, 200–205.
- Zhang, X., Ren, W., DeCaen, P., Yan, C., Tao, X., Tang, L., Wang, J., Hasegawa, K., Kumasaka, T., He, J., et al. (2012). Crystal structure of an orthologue of the NaChBac voltage-gated sodium channel. *Nature* *486*, 130–134.

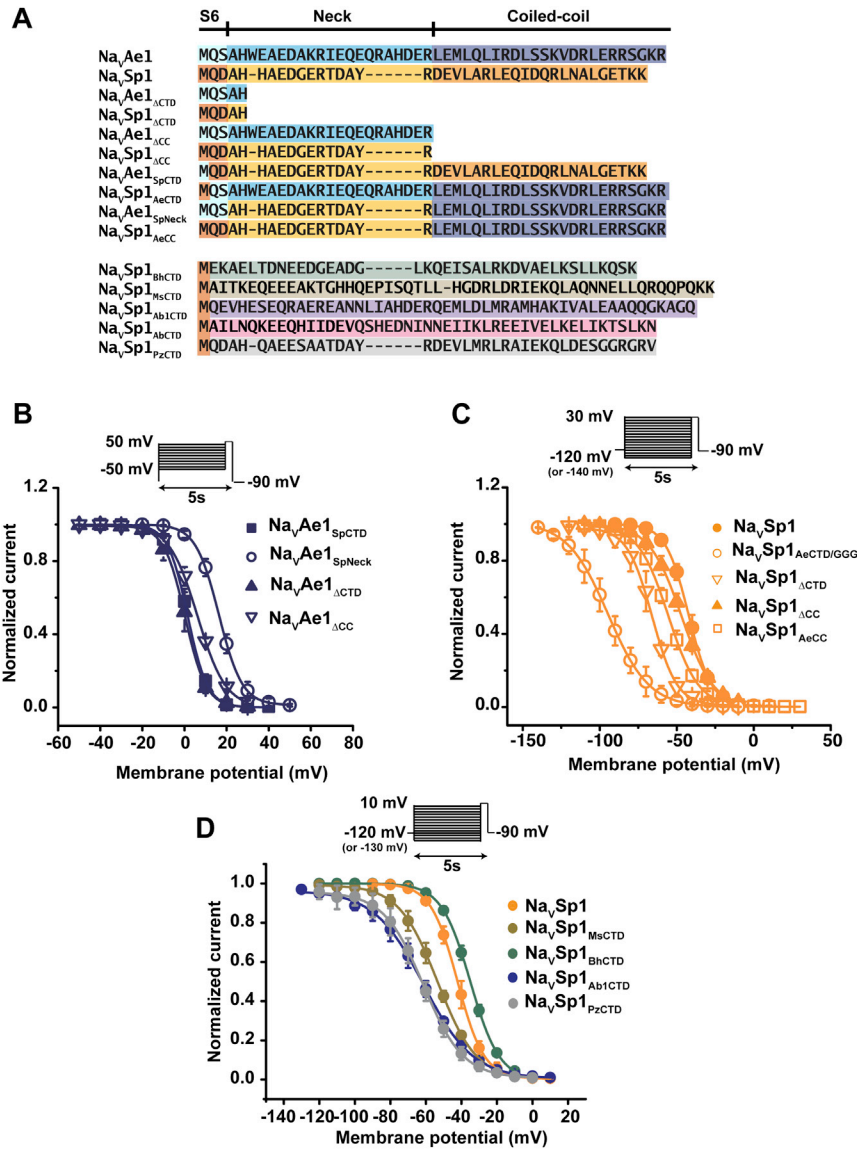


Figure S1. BacNa_v Chimeras and Deletions, Related to Figures 1 and 2

(A) BacNa_v deletion and chimera sequence map. Colors indicate the origins of the various elements: Na_vAe1, S6 (cyan), neck (light blue), coiled-coil (slate); Na_vSp1, S6 (dark orange), neck (yellow orange), coiled-coil (light orange); Na_vBh1 CTD (dark green); Na_vMs CTD (tan); Na_vAb1 CTD (purple); Na_vAb CTD (pink); and Na_vPz CTD (gray).

(B–D) Voltage dependent inactivation curves for indicated chimeras and mutants: (B) Na_vAe1 CTD chimeras and mutants; (C) Na_vSp1 CTD chimeras and mutants; and (D) Na_vSp1 CTD chimeras. Voltage step protocol is shown for (B)–(D).

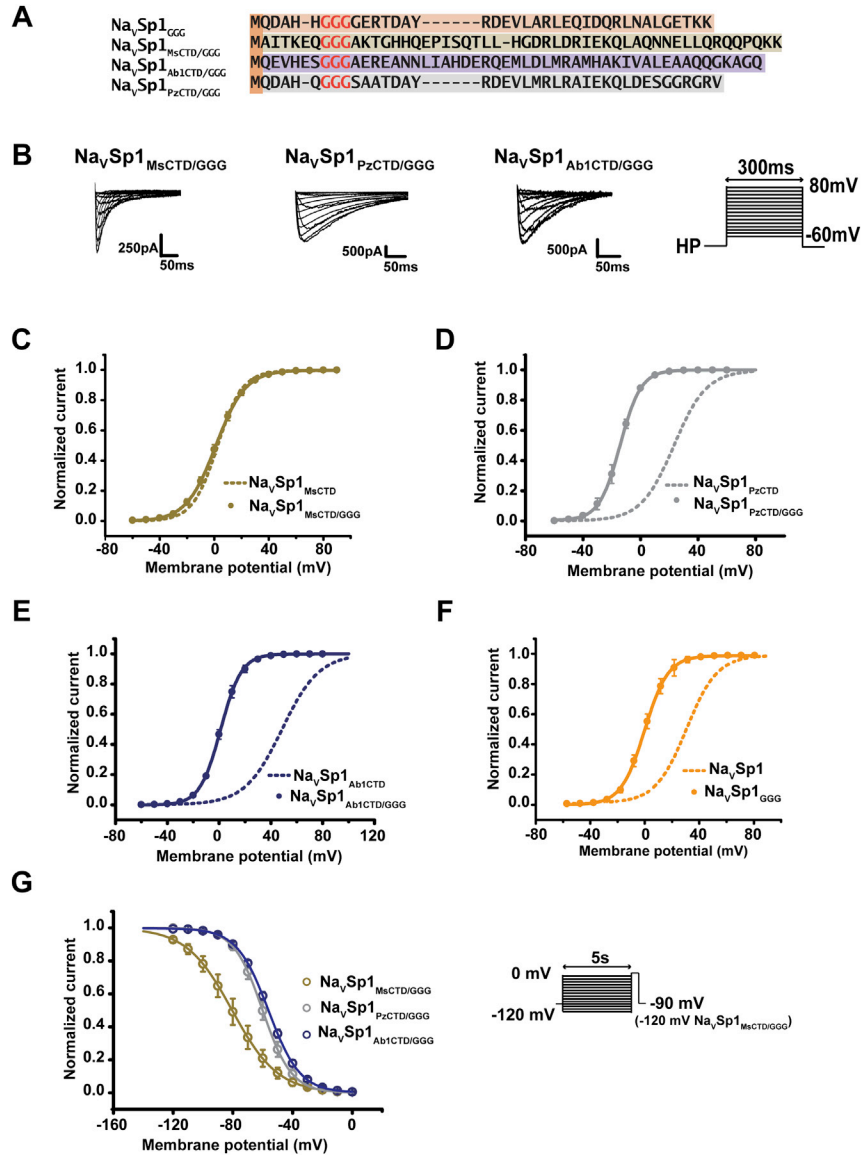


Figure S2. BacNa_v GGG Mutants, Related to Figure 2

(A) BacNa_v sequences showing location of GGG mutations (red).

(B) Exemplar currents for Na_vSp1_{MsCTD/GGG}, Na_vSp1_{PzCTD/GGG}, and Na_vSp1_{Ab1CTD}. Voltage step protocol is shown. Holding potential (HP) was 5 s at -90 mV (-120 mV for Na_vSp1_{MsCTD/GGG}).

(C-F) Voltage dependent activation curves for (C) Na_vSp1_{MsCTD/GGG}, (D) Na_vSp1_{PzCTD/GGG}, (E) Na_vSp1_{Ab1CTD/GGG} and (F) Na_vSp1_{GGG}. Dashed lines show the voltage dependent activation curves for the parent channels.

(G) Voltage dependent inactivation curves for Na_vSp1_{MsCTD/GGG} (tan), Na_vSp1_{PzCTD/GGG} (gray), and Na_vSp1_{Ab1CTD/GGG} (blue). Voltage step protocol is shown.

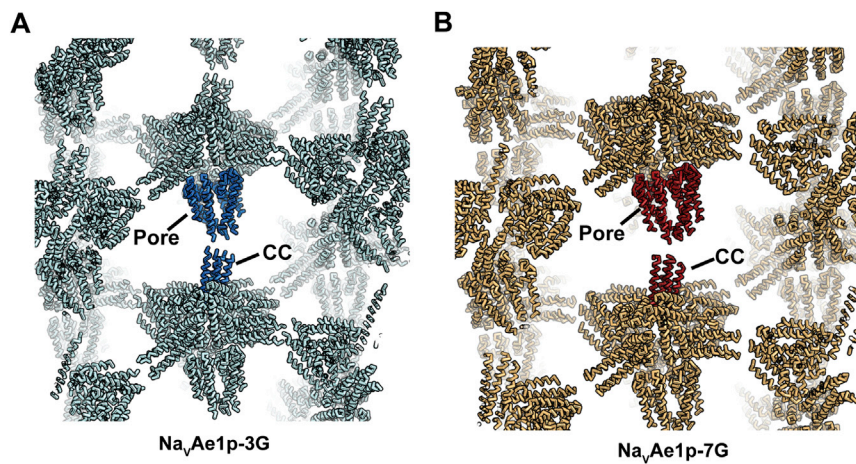


Figure S3. Crystal Lattice Packing, Related to Figure 3

(A and B) In each case, (A) Na_vAe1p-3G and (B) Na_vAe1p-7G, the asymmetric unit is shown surrounded by lighter colored symmetry related molecules. Transmembrane pore domain (Pore) and coiled-coil (CC) domain are indicated.

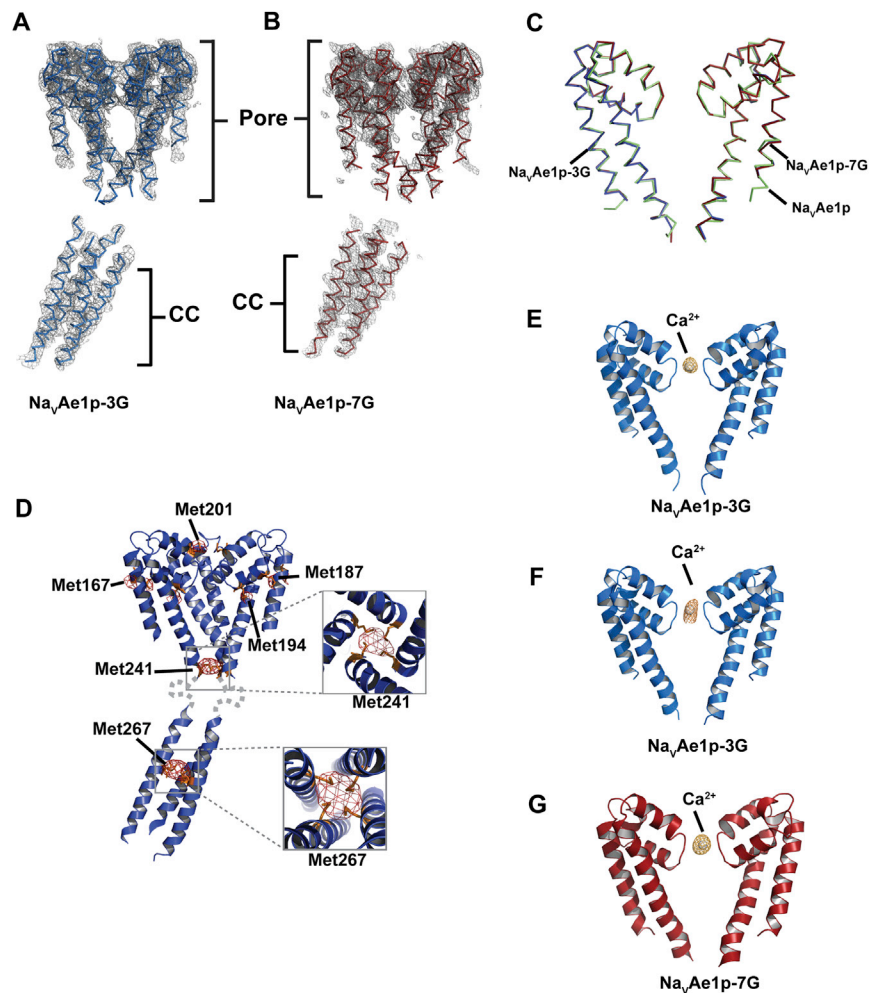


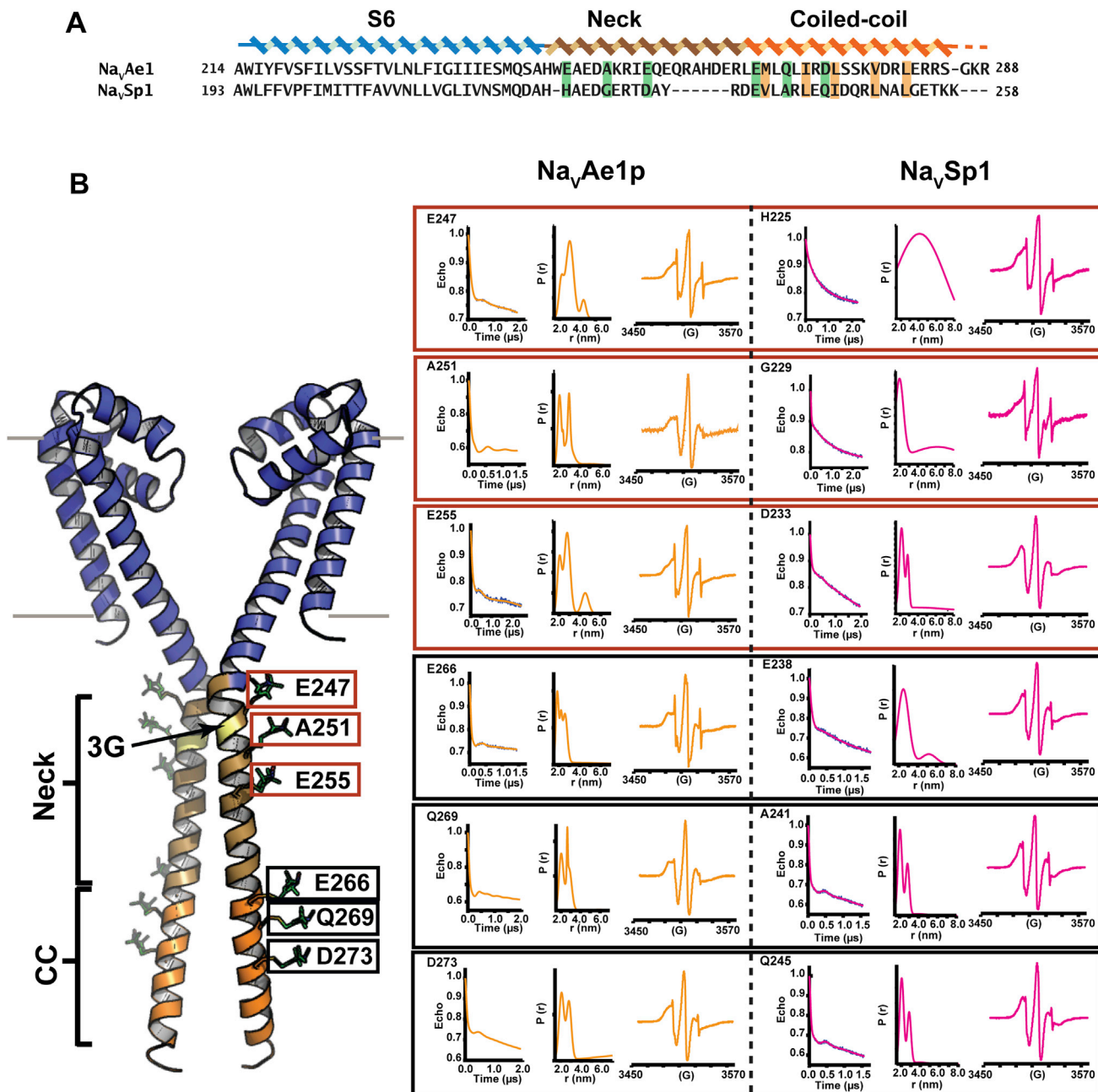
Figure S4. $\text{Na}_v\text{Ae1p-3G}$ and $\text{Na}_v\text{Ae1p-7G}$ Structural Features, Related to Figure 3

(A and B) Electron density (1.5σ) for (A) $\text{Na}_v\text{Ae1p-3G}$ (marine) and (B) $\text{Na}_v\text{Ae1p-7G}$ (firebrick). Pore and coiled-coil (CC) domains are indicated.

(C) Superposition of the pore domains of $\text{Na}_v\text{Ae1p}$ (4LTO) (lime green), $\text{Na}_v\text{Ae1p-3G}$ (marine), and $\text{Na}_v\text{Ae1p-7G}$ (firebrick).

(D) Anomalous difference maps for SeMet labeled $\text{Na}_v\text{Ae1p-3G}$ (5σ). Insets show Met241 and Met267 viewed along the central axis.

(E–G) Density for pore ions in the (E) $\text{Na}_v\text{Ae1p-3G}$ pore domain Fo-Fc map (5σ), (F) $\text{Na}_v\text{Ae1p-3G}$ pore domain anomalous difference map (3σ), and (G) $\text{Na}_v\text{Ae1p-7G}$ pore domain Fo-Fc map (5σ). In (E) and (F) the ion is assigned as Ca^{2+} based on the anomalous difference density. The ion in (G) is also likely to be Ca^{2+} based on similarity with $\text{Na}_v\text{Ae1p-3G}$ and the 50 mM CaCl_2 in the crystallization conditions Ca^{2+} .



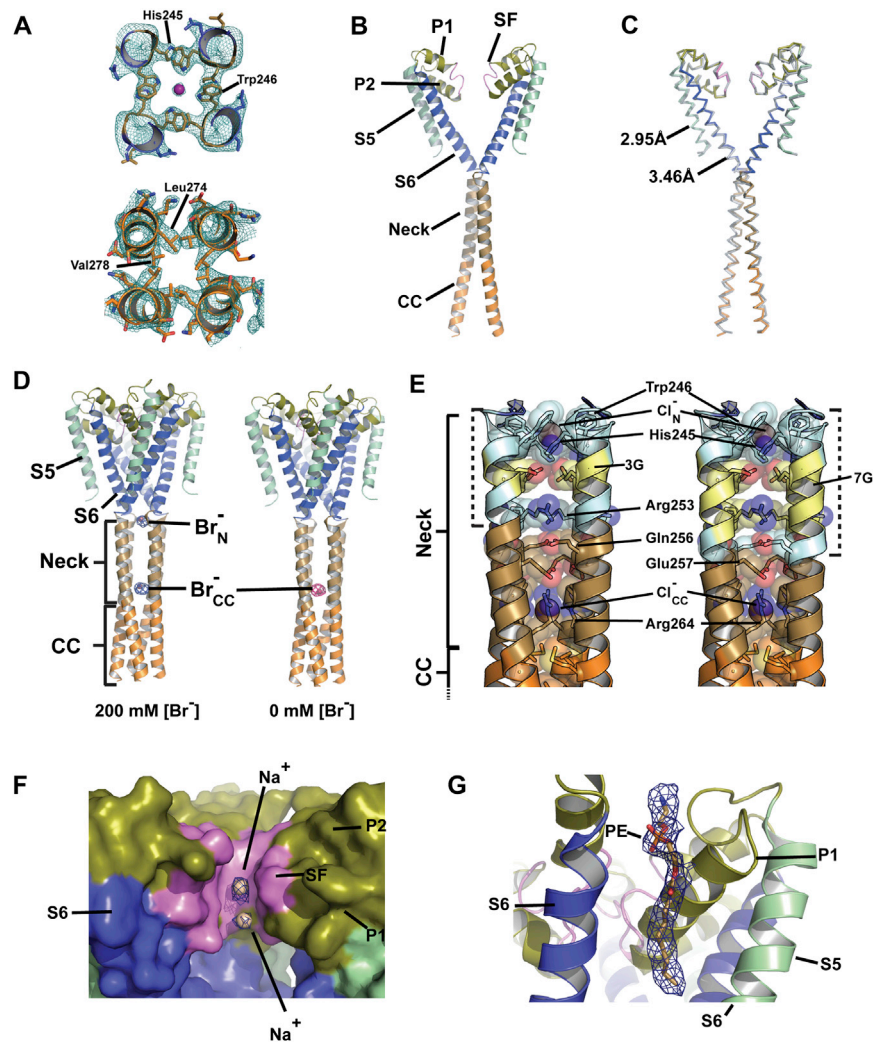


Figure S6. Structural Features of Na_vAe1p at 2.95 Å Resolution, Related to Figure 5

(A) Exemplar electron density (1.5σ) for π -stack (top) and coiled-coil (bottom) regions of Na_vAe1p at 2.95 Å. Select residues are indicated.

(B) Cartoon representation of the overall structure of Na_vAe1p determined at 2.95 Å. Secondary structure elements are indicated and colored as follows: S5 (green), P1 and P2 helices (olive), selectivity filter (SF, violet), S6 (blue), neck (tan) and coiled-coil (CC, orange). Two subunits are shown.

(C) Superposition of Na_vAe1p determined at 2.95 Å (colored as in A) and 3.46 Å (4LTO) (gray) (Shaya et al., 2014). $RMSD_{C\alpha} = 1.0$ Å (monomer) and 1.2 Å (tetramer).

(D) Anomalous difference maps (5σ) calculated at 5 Å for Na_vAe1p crystallized using 200mM NaBr and either soaked in cryo-protectant solution with 200 mM NaBr (left panel) or 0 mM NaBr (right panel). Anomalous signal for the neck ion, Br_N⁻, and coiled-coil ion, Br_{CC}⁻, are indicated.

(E) Cartoon diagram showing location of 3G and 7G substitutions (yellow). Extent of the disordered regions in Na_vAe1p-3G (left) and Na_vAe1p-7G (right) is indicated in cyan and by the bracketed dashes.

(F) $2F_{O}-F_{C}$ density (1.0σ) for Na_vAe1p selectivity filter ions. Channel elements are labeled and colored as (A). The front monomer is removed for clarity.

(G) $2F_{O}-F_{C}$ density (1.0σ) for the position of an intersubunit bound lipid, modeled as phosphoethanolamine. Density for one acyl chain is defined.

Cell, Volume 164

Supplemental Information

Unfolding of a Temperature-Sensitive Domain

Controls Voltage-Gated Channel Activation

Cristina Arrigoni, Ahmed Rohaim, David Shaya, Felix Findeisen, Richard A. Stein, Shailika Reddy Nurva, Smriti Mishra, Hassane S. Mchaourab, and Daniel L. Minor, Jr.

Supplemental material for:

Unfolding of a temperature-sensitive domain controls voltage-gated channel activation

Cristina Arrigoni^{1‡}, Ahmed Rohaim^{1,2‡}, David Shaya¹, Felix Findeisen¹, Richard A. Stein³, Shailika Reddy Nurva¹, Smriti Mishra³, Hassane S. Mchaourab³, and Daniel L. Minor, Jr^{1, 4, 5, 6*}

¹Cardiovascular Research Institute

⁴Departments of Biochemistry and Biophysics, and Cellular and Molecular Pharmacology

⁵California Institute for Quantitative Biomedical Research

University of California, San Francisco, California 94158 USA

⁶Physical Biosciences Division

Lawrence Berkeley National Laboratory, Berkeley, CA 94720 USA

³Department of Molecular Physiology and Biophysics

Vanderbilt University, Nashville, TN 37232

²Department of Biophysics

Faculty of Science

Cairo University, Giza, Egypt

[‡]Equal contributions

*Corresponding author: daniel.minor@ucsf.edu

Contents:

Supplemental Experimental procedures

Supplemental Tables S1-S5

Supplemental References

Supplemental Experimental Procedures

Construct design and cloning

For the CTD chimeras, NavSp1 and NavAe1 transmembrane regions covered residues 1 to 220 and 1 to 241, respectively, and the CTDs covered residues 221 to 258 and 242 to 288, respectively. For NavAe1_{SpNeck}, the NavAe1 transmembrane residues 1-241 were joined to a CTD comprising NavSp1 neck residues 222-236 and NavAe1 coiled-coil residues 265-288. For NavSp1_{AeCC}, NavSp1 residues comprising the transmembrane regions and neck 1-236 were joined to NavAe1 coiled-coil residues 265-288. CTDs from other BacNavs, NavMs (222 to 272), *Bacillus halodurans* NavBh1 (236 to 274) (Ren et al., 2001), *Arcobacter butzleri* NavAb (222 to 283) (Payandeh et al., 2011), *Alcanivorax borkumensis* NavAb1 (234 to 283) (Shaya et al., 2011), and *Paracoccus zeaxanthinifaciens* (233 to 262) (Koishi et al., 2004) were fused to the NavSp1 transmembrane region spanning residues 1-220. The CTD cDNAs for NavAb, NavBh1, NavPz, and NavAb1 were obtained by PCR from the genomic DNA (ATCC). cDNA for the NavMs CTD was generated by *in vitro* gene synthesis (Gene2Oligo).

Patch-clamp electrophysiology

Overexpression and patch-clamp recording from NavSp1, NavAe1, mutants, and chimeras were performed as described (Shaya et al., 2014). Pipette solution contained, in mM: 120 Cs-methane sulfonate, 8 NaCl, 10 EGTA, 2 Mg-ATP, and 20 HEPES (pH 7.4 with CsOH). Bath solution contained, in mM: 155 NaCl, 1 CaCl₂, 1 MgCl₂, 5 KCl, 10 glucose, 10 HEPES (pH 7.4 with NaOH). Currents were elicited with a voltage step protocol that is schematically represented in Figures 1 and 2. For NavAe1_{H245G}, NavAe1_{W246G}, and NavAe1_{H245G/W246G} currents were recorded with a voltage step protocol using 600 ms 10 mV steps from -10 mV to +80 mV. For voltage dependent inactivation, 5 s 10 mV step pre-sweeps from +50 mV to -40 mV preceded a +50 mV test step. In both protocols every sweep was followed by 5 s at -90mV. For NavSp1, NavSp1_{GGG}, NavSp1_{M220A}, NavSp1_{M220A/GGG}, NavSp1_{R1Q}, NavSp1_{R1Q/GGG}, NavSp1_{R2Q/GGG}, NavSp1_{R3Q}, NavSp1_{R3Q/GGG}, NavSp1_{R4Q}, and NavSp1_{R4Q/GGG} currents were elicited by a 300ms (600ms for NavSp1_{R3Q/GGG}) 10 mV step protocol from -60 mV to +80mV. NavSp1_{R2Q} currents were recorded with a P/-4 10 mV step protocol from +30 mV to +170 mV. Holding potential was -90mV (-100 mV for NavSp1_{R3Q/GGG}). For temperature-dependence experiments, the bath solution was held at the desired temperature with a CL-100 bipolar temperature controller (Warner Instruments) coupled to a SC-20 Dual In-line Solution Heater/Cooler (Warner Instruments). The value for NavSp1_{Ab1CTD} at 18°C could not be measured due to low current amplitude. Voltage dependence was analyzed with the Boltzmann equation, $y = 1/(1 + \exp[(V-V_{1/2})/s])$, where y is fractional activation, V is voltage, V_{1/2} half-activation voltage and s is the inverse slope factor (mV). Data were analyzed with Clampfit 10.3 (Molecular Devices) and Origin (OriginLab Corp.).

Surface biotinylation assay

70%-confluent HEK 293 cells plated on a 10 cm² dish were transfected with 8 µg of DNA for each HA-tagged construct in pIRES-EGFP and 20 µl of Lipofectamine 2000 (Invitrogen). Assay was performed at 4°C, and all

solutions were pre-cooled on ice. After 24 hrs cells were washed 3x with Phosphate buffered saline (PBS) at pH 7.4 (Gibco, #10010023) and incubated (20' at 4°C) with 0.5 mM of Sulfo-NHS-SS-biotin (ThermoScientific) dissolved in water. Cells were then washed 3x with PBS and the biotinylation reaction was quenched with 100mM Glycine, 0.5% BSA in PBS pH7.4 for 10'. Cells were then washed 3x with 100 mM Glycine, PBS pH 7.4. After the last wash, all buffer was carefully removed and cells in each plate were resuspended in 0.5 mL of Lysis Buffer (PBS, 5mM EDTA, 1% Triton X-100, 1 Complete protease inhibitor tablet (Roche)). Cells were gently passed through a 21G needle and incubated on ice for 20'. Debris was removed by centrifugation (10,000 x g, 15'). Supernatant (~0.5 ml) was incubated with gentle shaking with 50 µl of Streptavidin Agarose beads (Pierce, #20357) (2 hrs, 4°C) and unbound material was collected. Labeled proteins were eluted with a 10' incubation with Laemmli buffer supplemented with 20% β-mercaptoethanol. Unbound and elution fractions were analyzed on SDS-PAGE and Western Blot detected by Western Lightning ECL (PerkinElmer) after incubation with a mouse monoclonal anti-HA tag antibody (HA-7 clone, Sigma-Aldrich) and a secondary HRP-linked anti-mouse antibody (Cell Signaling, #7076S). Green Fluorescent protein (GFP) was detected with a rabbit anti-GFP antibody (Cell Signaling, #2555S) and a secondary HRP-linked anti-rabbit antibody (Cell Signaling, #7074S).

Protein purification and crystallization

Na_vAe1p

Purified Na_vAe1p was concentrated to 10 mg ml⁻¹ using an Amicon® Ultra-15 concentrator (100-kDa MW cutoff, Millipore). Crystals were grown using hanging drop vapor diffusion over 27% PEG 300, 100 mM Na-acetate, pH 5.5, at 4°C in a 24 well VDX Plate™ (Hampton research) using a 1:1 ratio of protein:mother liquor. Orthorhombic crystals appeared overnight, were harvested after five days, and frozen directly into liquid N₂ following addition 1 µl 100 mM NaAc pH 5.5, 35 % PEG 300 to the drop.

For samples containing NaBr, a final size-exclusion chromatography buffer of 200 mM NaBr, 0.3 mM DDM, 20 mM Na-HEPES, pH 8.0 was used prior to concentration. High NaBr-containing crystals were grown from a solution of 13.5 mg ml⁻¹ protein over a reservoir of 100 mM Na-acetate, pH 5.25, 30% PEG 300. Crystals appeared overnight and after 5 days were frozen directly into liquid N₂. To produce Low NaBr crystals, crystals were grown using the same protein for the High NaBr crystals over a reservoir of 28% PEG 300, 100 mM Na acetate, pH 4.9. Orthorhombic crystals grew overnight and were harvested after 3 days. Prior to freezing, crystals were cryo-protected by passage through mother liquor solutions in which PEG300 concentration was increased to 35% using three 2% increments and one 1% increments. At each step the crystals were briefly soaked in the new solution. Following the final 1% step, the crystals were frozen in liquid N₂ for data collection.

Na_vAe1p-3G and Na_vAe1p-7G

Cells were grown in 2YT medium supplemented with 25 µg ml⁻¹ kanamycin inoculated with a 1:100 dilution of a saturated overnight culture. Cells were grown at 37°C to OD₆₀₀=0.6, after which protein expression was induced with 0.35 mM Isopropyl β-D-1-thiogalactopyranoside (IPTG) at 20°C for 24 hours. Cells were

harvested by centrifugation (6,000 x g, 15'), frozen in liquid N₂, and stored at -80°C. Cell pellets were resuspended in cold lysis buffer (500 mM NaCl, 2 mM phenylmethylsulfonyl fluoride (PMSF) 50 mM Tris-HCl pH 8.0) and disrupted using an EmulsiFlex-C5 homogenizer (Avestin). The lysate was then centrifuged to remove debris and unbroken cells (12,000 x g, 1 hr). The soluble fraction was collected and the membranes were isolated by ultracentrifugation (160,000 x g, 2 hr). After ultracentrifugation, the supernatant was discarded, and the membrane pellet was homogenized in membrane suspension buffer (200 mM NaCl, 8% glycerol, 50 mM Tris-HCl pH 8.0) using dounce tissue grinder (Kimble Kontes LLC). Membrane proteins were solubilized addition of n-dodecyl-β-D-maltopyranoside (β-DDM, Anatrance) to 40 mM and incubated for 2 hrs at 4°C. Ultracentrifugation (160,000 x g, 30') was then used to harvest the soluble fraction. Solubilized Na_vAe1p-3G or Na_vAe1p-7G was loaded onto a PorosMC nickel affinity column (Applied Biosystems) pre-equilibrated with loading buffer (20 mM Imidazole, 200 mM NaCl, 0.3 mM β-DDM, 8 % glycerol, 20 mM Tris-HCl pH 8.0). Unbound material was removed by washing with 5 column volumes (CV) of loading buffer. Bound material was eluted using 2 CV of elution buffer (300 mM imidazole, 200 mM NaCl, 0.3 mM β-DDM, 8 % glycerol, 20 mM Tris-HCl pH 8.0.). The HM3C affinity tag was cleaved by addition of purified His₆-3C protease (Cordingley et al., 1990) and DTT to a final concentration of 1 mM followed by incubation for 6 hr at 4°C with gentle agitation. Imidazole and DTT were removed by HiPrep 26/10 Desalting column (GE Healthcare) run in 200 mM NaCl, 8% glycerol, 0.3 mM β-DDM, 20 mM Tris-HCl pH 8.0. The cleaved tag was removed by passing the mixture through a PorosMC nickel affinity column run in series with a pre-packed Amylose affinity column (NEB). Flowthrough containing the cleaved protein was collected and passed over a HiPrep 26/10 Desalting column run in Buffer A (20 mM NaCl, 0.3 mM β-DDM, 8 % glycerol, 20 mM Tris-HCl pH 8.0,) after which the protein was loaded onto a PorosQ column (Applied Biosystems) pre-equilibrated with Buffer A. Protein was eluted using a linear gradient from 20 mM to 500 mM NaCl over 20 CV using Buffer B (500 mM NaCl, 0.3 mM β-DDM, 8 % glycerol, 20 mM Tris-HCl pH 8.0.), concentrated using an Amicon Ultra-15 centrifugal filtration device (50-kDa MW cutoff, Millipore, and loaded onto size exclusion column (Superdex 200 10/300 GL, GE Healthcare) run in 200 mM NaCl, and 0.3 mM DDM, 20 mM Hepes pH 8.0.

Na_vAe1p-3G Selenomethionine labeling

To produce selenomethionine labeled Na_vAe1p-3G, a 10 ml culture of *E. coli* (DE3) pLysS C43 harboring the expression plasmid for Na_vAe1p-3G was grown overnight in Luria-Bertani (LB) medium containing 25 μg ml⁻¹ Kanamycin at 37°C. 10 ml of saturated culture was split into 10 aliquots that were each centrifuged (13,000 x g, 2') using a table-top centrifuge. The supernatant was discarded, and the pellet was resuspended in sterile filtered M9 minimal medium. Each 1 ml aliquot was used to inoculate 1L of M9 minimal medium supplemented with 25 μg ml⁻¹ kanamycin and grown in a shaker at 37°C degrees. Once OD₆₀₀=0.6 was reached, 100 mg L⁻¹ of L-lysine, L-threonine and L-phenylalanine, 50 mg L⁻¹ of L-isoleucine, L-leucine, L-valine, and 60 mg L⁻¹ of L-SeMet were added. After 15' of shaking, the temperature was reduced to 30°C, IPTG to 0.35 mM was added and the culture was grown for 24 hours. Cells were harvested (6,000 x g, 15', 4°C), frozen in liquid nitrogen, and stored at -80°C. SeMet labeled protein was purified as described above.

Prior to crystallization, purified Na_vAe1p-3G, Na_vAe1p-3G SeMet, and Na_vAe1p-7G were exchanged into 150 mM NaCl, 50 mM CaCl₂, 0.3 mM β-DDM, 20 mM HEPES pH 8.0 using a Superdex200 10/300 (GE Healthcare) column and concentrated to 12 mg ml⁻¹ using an Amicon Ultra-15 concentrator (100-kDa MW cutoff, Millipore). Crystals were grown by microbatch under 100 μl paraffin oil for Na_vAe1p-3G (12 mg ml⁻¹, 30% PEG 400, 20 mM MES pH 5.4), Na_vAe1p-7G (12 mg ml⁻¹, 30 % PEG 400, 20 mM MES pH 5.8) at 4°C, and Na_vAe1p-3G SeMet (8 mg ml⁻¹, 30% PEG 400, 100 mM MES pH 6.6) at 4°C. Crystals were harvested using a final concentration of 35 % PEG 400 before freezing in liquid N₂.

Data collection, structure determination, and refinement

Diffraction data for Na_vAe1p, Na_vAe1p-NaBr complexes, and Na_vAe1p-3G SeMet were collected at Advanced Photon Source Beamline 23ID-B, Argonne National Laboratory. For the NaBr containing crystals, data collection was performed at the Br⁻ edge, determined on-site at 13.476 keV (0.92 Å) from a fluorescence scan using a Na_vAe1p crystal co-crystallized and frozen in high NaBr. Diffraction images were integrated using iMOSFLM 1.0.5 (Battye et al., 2011), and scaled with SCALA (3.3.20) (Evans, 2011). Data were refined with Refmac (5.6.0117)(Murshudov et al., 2011) against the initial model of Na_vAe1p including only protein atoms. Anomalous maps were calculated using data merged in CCP4i (CAD) in Coot (Emsley and Cowtan, 2004). Map coefficients were exported from Coot and drawn using Pymol (The PyMOL Molecular Graphics System, Version 1.5.0.4 Schrödinger, LLC). Diffraction data for Na_vAe1p-3G and Na_vAe1p-7G were collected at Advanced Light Source Beamline 8.3.1, Lawrence Berkeley National Laboratory. Structures of Na_vAe1p-3G and Na_vAe1p-7G were solved by molecular replacement using the transmembrane portion of 4LTO as search model and Phaser (McCoy et al., 2007). Models were built and refined by multiple cycles using Coot and Refmac (5.6.0117)(Murshudov et al., 2011) in which NCS restraints were applied throughout the refinement.

EPR labeling and sample preparation

Na_vAe1p, Na_vAe1p-3G, and Na_vSp1p have no naturally occurring cysteines. Single cysteine point mutants were generated by quick-change mutagenesis. Each BacNa_v mutant was purified as above with the addition of 1 mM TCEP in all the buffers. To ensure reduction of the cysteines, an additional 2 mM DTT was added to the samples prior to labeling. TCEP and DTT were removed on a GE HiTrap column. Samples from the desalting column were incubated with MTSSL at a 30:1 label/protein molar ratio for 1.5 h at room temperature. A second addition of MTSSL at 20:1 was made and incubated for an additional 1.5 h at room temperature. A final 20:1 addition of MTSSL was made and the sample was incubated at 4 °C overnight. Excess MTSSL reagent was removed by gel filtration with a Superdex 200 10/300 GE column. CW-spectra were collected on a Bruker EMX at 10 mW power with a modulation amplitude of 1.6G. All spectra were normalized to the double integral. DEER experiments were carried out using a standard four-pulse protocol (Jeschke, 2002). DEER distributions were obtained from global analysis of DEER decays (Brandon et al., 2012; Mishra et al., 2014; Stein et al., 2015)

Table S1, Related to Figures 1 and 2

BacNav_v activation and inactivation properties

	V _{1/2, act}	ΔV _{1/2, act}	n	V _{1/2, inact}	ΔV _{1/2, inact}	n
NavAe1	-	-		-	-	
NavAe1_{ΔCTD}	19.1 ± 1.9	-	5	1.0 ± 1.8	-	5
NavAe1_{ΔCC}	17.4 ± 1.7	-1.7 ± 4.7*	6	4.18 ± 2.1	3.2 ± 5.2*	4
NavAe1_{SpCTD}	38.8 ± 2.5	19.7 ± 5.9*	6	3.5 ± 1.7	2.5 ± 4.6*	5
NavAe1_{SpNeck}	32.7 ± 2.0	13.6 ± 5.1*	6	18.2 ± 1.9	17.2 ± 5.4*	5
NavAe1_{GGG}***	32.1 ± 1.1	13 ± 3.9*	6	5.3 ± 3.1	4.3 ± 6.4 *	4
NavSp1	28.9 ± 1.3	36.3 ± 5.4*	5	-41.6 ± 2.1	24.3 ± 5.8 *	4
NavSp1_{ΔCTD}	-7.4 ± 2.8	-	4	-65.9 ± 2.1	-	4
NavSp1_{ΔCC}	-9.7 ± 1.9	-2.3 ± 6.2*	5	-47.5 ± 1.3	18.4 ± 5.2*	4
NavSp1_{AeCTD}	-	-		-	-	
NavSp1_{AeCTD/GGG}	5.7 ± 2.6	13.1 ± 8.0*	3	-94.5 ± 0.1	-28.6 ± 5.8*	3
NavSp1_{AeCC}	26.1 ± 1.0	33.5 ± 5.8*	4	-56.0 ± 1.6	9.9 ± 5.4**	4
NavSp1_{GGG}	-10.5 ± 2.1	-39.4 ± 4.6**	5	-60.8 ± 1.9***	-18.1 ± 3.6***	10
NavSp1_{Bh1CTD}	-15.6 ± 1.9	-44.5 ± 4.4**	6	-37.9 ± 3.1	3.7 ± 7.3**	4
NavSp1_{MsCTD}	1.6 ± 1.6	-27.3 ± 3.8**	5	-50 ± 2.6	-8.4 ± 6.6**	5
NavSp1_{MsCTD/GGG}	2.5 ± 1.0	0.9 ± 3.2 [#]	7	-80.5 ± 4.4	-30.7 ± 7.7 [#]	3
NavSp1_{Ab1CTD}	49.3 ± 3.1	20.4 ± 5.8**	4	-61 ± 2.5	-19.4 ± 6.3 **	4
NavSp1_{Ab1CTD/GGG}	2.1 ± 1.1	-47.2 ± 5.2 [#]	6	-56.2 ± 0.9	4.8 ± 6.2 [#]	3
NavSp1_{PzCTD}	24.7 ± 0.9	-4.2 ± 2.8**	6	-63.3 ± 3.3	-21.7 ± 7.6**	4
NavSp1_{PzCTD/GGG}	-14.6 ± 1.4	-39.3 ± 3.1 [#]	3	-60.0 ± 2.0	3.3 ± 8.5 [#]	3
NavSp1_{AbCTD}	-	-		-	-	
NavAe1_{H245G}	46.4 ± 0.5	-	3	13.7 ± 1.2	-	3
NavAe1_{W246G}	47.2 ± 0.3	-	3	11.9 ± 1.2	-	4
NavAe1_{H245G/W246G}	42.4 ± 0.2	-	4	14.8 ± 2.6		3

*ΔV_{1/2, act} and ΔV_{1/2, inact} are calculated relative to the values of the constructs in which the entire CTD is deleted.

**ΔV_{1/2, act} and ΔV_{1/2, inact} are calculated relative to NavSp1.

[#]ΔV_{1/2, act} calculated relative to the parent NavSp1 chimera.

*** Values from (Shaya et al., 2014)

ΔCTD = NavAe1 Δ(246-288) and NavSp1 Δ(225-258)

ΔCC = NavAe1 Δ(269-288) and NavSp1 Δ(237-258)

Data are mean ± s.e.m.

ΔV_{1/2} '±' denotes 90% confidence interval

Table S2, Related to Figure 2

Temperature dependence of $V_{1/2}$ activation of $\text{Na}_v\text{Sp1}$ mutants and chimeras

	$V_{1/2, \text{act}}$ 18°C	$V_{1/2, \text{act}}$ 23°C	$V_{1/2, \text{act}}$ 30°C	$V_{1/2, \text{act}}$ 35°C	$\Delta V_{1/2, \text{act}}$ ($V_{18}-V_{35}$)
$\text{Na}_v\text{Sp1}$	41.3 ± 3.6 (5)	28.7 ± 1.2 (5)	11.6 ± 1.5 (3)	4.7 ± 1.6 (3)	36.6 ± 9.6
$\text{Na}_v\text{Sp1}_{\text{ACTD}}$	-10.7 ± 0.9 (3)	-11.1 ± 3.1 (4)	-6.4 ± 2.7 (3)	-6.8 ± 3.2 (3)	-3.9 ± 7.1
$\text{Na}_v\text{Sp1}_{\text{GGG}}$	-15.6 ± 1.8 (3)	-10.9 ± 1.8 (5)	-12.2 ± 1.7 (4)	-9.7 ± 1.3 (3)	-5.9 ± 4.7
$\text{Na}_v\text{Sp1}_{\text{BH1CTD}}$	-17.0 ± 2.0 (3)	-13.9 ± 1.8 (4)	-13.4 ± 2.0 (3)	-17.6 ± 0.9 (3)	0.6 ± 4.7
$\text{Na}_v\text{Sp1}_{\text{MSCTD}}$	2.8 ± 0.9 (3)	-0.4 ± 0.9 (5)	2.8 ± 5.2 (4)	2.0 ± 1.7 (3)	0.8 ± 4.1
$\text{Na}_v\text{Sp1}_{\text{Ab1CTD}}$	n.a.	48.6 ± 1.0 (4)	33.5 ± 1.5 (3)	13.9 ± 0.9 (3)	34.7 ± 2.8*
$\text{Na}_v\text{Sp1}_{\text{PzCTD}}$	34.0 ± 3.0 (3)	24.8 ± 1.4 (4)	14.9 ± 0.3 (3)	8.5 ± 1.5 (3)	25.5 ± 7.1

Data are mean ± s.e.m.

N value is indicated in parenthesis.

$\Delta V_{1/2}$ '±' denotes 90% confidence interval

* $\Delta V_{1/2, \text{act}}$ for $\text{Na}_v\text{Sp1}_{\text{Ab1CTD}}$ is calculated as ($V_{23}-V_{35}$).

Table S3, Related to Figures 3 and 5
Crystallographic data collection and refinement statistics

	NavAe1p-3G	NavAe1p-3G SetMet	NavAe1p-7G	NavAe1p	NavAe1p High Br ⁻	NavAe1p Low Br ⁻
Data collection						
Wavelength	1.1158	0.9795	1.0332	0.9999	0.9200	0.9200
Space group	I222	I222	I222	I222	I222	I222
Cell dimensions						
<i>a, b, c</i> (Å)	138.31, 153.35, 165.81	144.35, 150.19, 167.38	137.10, 138.99, 173.16	153.51, 160.52, 166.37	157.40, 160.87, 167.35	151.72, 159.95, 168.57
α, β, γ (°)	90, 90, 90	90, 90, 90	90, 90, 90	90, 90, 90	90, 90, 90	90, 90, 90
Resolution (Å)	50 - 3.70 (3.78 - 3.70)	50 - 5.50 (5.69 - 5.50)	68.60 - 3.80 (3.93 - 3.80)	80.26 - 2.95 (3.11-2.95)	56.25-3.75 (3.95 - 3.75)	62.49 - 3.33 (3.51 - 3.33)
<i>R</i> _{pim} (%)	4.3 (118.0)	4.3 (86.3)	1.6 (171.4)	9.9 (143.4)	8.8 (110.3)	8.0 (80.2)
<i>Mn I / σ</i>	8.91 (0.70)	8.4 (1.0)	6.22 (0.90)	6.7 (0.6)	5.8 (0.9)	8.7 (1.0)
CC _{1/2}	1.0 (0.221)	0.974 (0.163)	0.99 (0.049)	0.995 (0.126)	0.998 (0.098)	0.998 (0.112)
Completeness (%)	99.86 (99.85)	99.5 (99.9)	97.48 (98.34)	99.2 (100.0)	98.8 (99.8)	98.6 (98.7)
Multiplicity	14.0 (14.1)	6.4 (6.5)	3.9 (4.0)	8.5 (8.5)	4.6 (4.6)	8.5 (8.5)
Unique No. reflections	19966	15594	18097	21986	28089	29811
Refinement						
<i>R</i> _{work} / <i>R</i> _{free} (%)	27.3 / 30.3	25.7 / 28.8	27.2 / 31.1	20.4 / 23.9	22.8 / 28.0	21.2 / 26.2
Resolution (Å)	15.0 - 3.7	15.0 - 5.5	15.0 - 3.8	15.5 - 2.95	15.0 - 3.75	15.0 - 3.33
No. of chains in AU	4	4	4	4	4	4
No. atoms	3879	3765	3768	4659	4502	4501
Protein	3738	3761	3760	4500	4500	4500
Selectivity filter ions	1	n/a	1	3	0	0
Halide ions	n/a	n/a	n/a	2	2	1
Lipid atoms	n/a	n/a	n/a	151	0	0
Water	4	4	7	3	0	0
<i>B</i> -factors						
Protein	143.60	344.50	156.10	93.14	169.51	113.12
Selectivity filter ions	265.85	n/a	160.12	93.66	n/a	n/a
Halide ions	n/a	n/a	n/a	93.5	187.16	131.98
Lipid atoms	n/a	n/a	n/a	106.52	n/a	n/a
Water	185.72	164.70	160.66	75.75	n/a	n/a
R.m.s. deviations						
Bond lengths (Å)	0.011	0.011	0.014	0.0180	0.0106	0.0127
Bond angles (°)	1.40	1.33	1.31	2.2	1.54	1.75
Ramachandran	90.9/0.0	84.5/0.4	86.2/0.0	93.7/0.0	98.0 / 0.0	97.3 / 0.0
most favored/disallowed (%)						

*Values in parentheses are for highest-resolution shell.

Table S4, Related to Figure 6

Activation properties of Na_vAe1 and Na_vSp1 coupling test mutants

	V _{1/2, act} (mV)	k (mV)	Z (e ₀)	n	ΔG° (kcal mol ⁻¹)	ΔΔG° _{obs} (kcal mol ⁻¹)	ΔΔG° _{calc} (kcal mol ⁻¹)	ΣΔG° (kcal mol ⁻¹)
Na_vSp1	27.7 ± 1.6	10.9 ± 0.5	2.3 ± 0.1	4	1.5 ± 0.4	-	-	-
Na_vSp1_{GGG}	-10.5 ± 2.1	7.8 ± 0.6	3.2 ± 0.3	5	-0.8 ± 0.3	-2.3 ± 0.9	-	-
Na_vSp1_{M220A}	-18.6 ± 2.7	9.3 ± 0.3	2.7 ± 0.3	7	-1.2 ± 0.4	-2.7 ± 1.1	-	-
Na_vSp1_{M220A/GGG}	-28.3 ± 4.0	10.1 ± 1.3	2.5 ± 0.3	4	-1.6 ± 0.6	-3.1 ± 1.4	-5.0 ± 2.7	1.9
Na_vSp1_{R1Q}	31.1 ± 1.2	10.4 ± 1.4	2.4 ± 0.3	4	1.7 ± 0.4	0.2 ± 1.1	-	-
Na_vSp1_{R1Q/GGG}	-9.2 ± 1.9	7.7 ± 1.4	3.2 ± 0.6	3	-0.7 ± 0.4	-2.2 ± 1.2	-2.1 ± 2.7	-0.1
Na_vSp1_{R2Q}	86.7 ± 1.2	10.7 ± 1.2	2.3 ± 0.3	4	4.6 ± 1.2	3.1 ± 2.5	-	-
Na_vSp1_{R2Q/GGG}	44.8 ± 2.1	11.5 ± 0.8	2.2 ± 0.2	4	2.3 ± 0.5	0.8 ± 1.2	0.8 ± 4.6	0.0
Na_vSp1_{R3Q}	11.7 ± 2.3	12.1 ± 1.6	2.1 ± 0.3	4	0.6 ± 0.3	-0.9 ± 1.0	-	-
Na_vSp1_{R3Q/GGG}	-24.5 ± 1.8	9.9 ± 0.9	2.5 ± 0.2	5	-1.4 ± 0.3	-2.9 ± 0.9	-3.2 ± 3.2	0.3
Na_vSp1_{R4Q}	59.9 ± 3.2	7.8 ± 0.7	3.2 ± 0.7	4	4.4 ± 1.9	2.9 ± 3.7	-	-
Na_vSp1_{R4Q/GGG}	32.7 ± 2.0	8.1 ± 0.5	3.1 ± 0.2	4	2.3 ± 0.4	0.8 ± 1.1	0.6 ± 6.5	0.2

Data are mean ± s.e.m.

For ΔG°, ΔΔG°_{obs}, and ΔΔG°_{calc} ± denotes 90% confident interval.

Z (e₀) is gating charge estimated from the mean value of slope factor from the Boltzmann fit (k), as $z = k^{-1}(RT/F)$, where RT/F = 25 mV.

ΔG° = ZV_{1/2}*0.02306, the free energy difference between the closed and open states at 0 mV.

ΔΔG°_{obs} = ΔG°_{mut} - ΔG°_{WT}, where ΔG°_{mut} - ΔG°_{WT} the measured values.

ΔΔG°_{calc} = ΔΔG°_X + ΔΔG°_Y, where ΔΔG°_X + ΔΔG°_Y are the free energy changes for the individual mutants.

ΣΔG° = ΔΔG°_{obs} - ΔΔG°_{pred}. Non-zero values indicate non-additive effects.

Table S5, Related to Figure 7**Coiled coil parameters**

Channel and element (residue numbers)	Na _v Ae1p* CC (265-285)	Na _v Ae1p CC (265-285)	Na _v Ae1p* neck + CC (247-285)	Na _v Ae1p neck + CC (247-285)	Na _v Ae1p* neck (247-264)	Na _v Ae1p neck (247-264)	TRPA1** CC
		2.95 Å		2.95 Å		2.95 Å	
Superhelical parameters							
Radius (Å)	7.4	7.4	7.6	7.8	8.1	8.3	8.0
Residues / superhelix turn	103	126	153	174	317	442	102
Superhelical Pitch (Å)	160	191	238	259	319	650	147.2
α-helical parameters							
Radius (Å)	2.24	2.22	2.27	2.24	2.30	2.26	2.13
Residues/turn	3.57	3.60	3.59	3.64	3.61	3.67	3.52
Rise/residue (Å)	1.57	1.51	1.55	1.49	1.52	1.47	1.45

Comparison of coiled-coil parameters as determined using Twister (Strelkov and Burkhard, 2002)

Calculated from PDB: *4LTO (Shaya et al., 2014) and ** 3J9P (Paulsen et al., 2015)

Supplemental References

- Battye, T.G., Kontogiannis, L., Johnson, O., Powell, H.R., and Leslie, A.G. (2011). iMOSFLM: a new graphical interface for diffraction-image processing with MOSFLM. *Acta Crystallogr D Biol Crystallogr* 67, 271-281.
- Brandon, S., Beth, A.H., and Hustedt, E.J. (2012). The global analysis of DEER data. *Journal of magnetic resonance* 218, 93-104.
- Cordingley, M.G., Callahan, P.L., Sardana, V.V., Garsky, V.M., and Colonno, R.J. (1990). Substrate requirements of human rhinovirus 3C protease for peptide cleavage in vitro. *J Biol Chem* 265, 9062-9065.
- Emsley, P., and Cowtan, K. (2004). Coot: model-building tools for molecular graphics. *Acta Crystallogr D Biol Crystallogr* 60, 2126-2132.
- Evans, P.R. (2011). An introduction to data reduction: space-group determination, scaling and intensity statistics. *Acta Crystallogr D Biol Crystallogr* 67, 282-292.
- Jeschke, G. (2002). Distance measurements in the nanometer range by pulse EPR. *Chemphyschem : a European journal of chemical physics and physical chemistry* 3, 927-932.
- Koishi, R., Xu, H., Ren, D., Navarro, B., Spiller, B.W., Shi, Q., and Clapham, D.E. (2004). A superfamily of voltage-gated sodium channels in bacteria. *J Biol Chem* 279, 9532-9538.
- McCoy, A.J., Grosse-Kunstleve, R.W., Adams, P.D., Winn, M.D., Storoni, L.C., and Read, R.J. (2007). Phaser crystallographic software. *J Appl Crystallogr* 40, 658-674.
- Mishra, S., Verhalen, B., Stein, R.A., Wen, P.C., Tajkhorshid, E., and McHaourab, H.S. (2014). Conformational dynamics of the nucleotide binding domains and the power stroke of a heterodimeric ABC transporter. *eLife* 3, e02740.
- Murshudov, G.N., Skubak, P., Lebedev, A.A., Pannu, N.S., Steiner, R.A., Nicholls, R.A., Winn, M.D., Long, F., and Vagin, A.A. (2011). REFMAC5 for the refinement of macromolecular crystal structures. *Acta Crystallogr D Biol Crystallogr* 67, 355-367.
- Paulsen, C.E., Armache, J.P., Gao, Y., Cheng, Y., and Julius, D. (2015). Structure of the TRPA1 ion channel suggests regulatory mechanisms. *Nature* 520, 511-517.
- Payandeh, J., Scheuer, T., Zheng, N., and Catterall, W.A. (2011). The crystal structure of a voltage-gated sodium channel. *Nature* 475, 353-358.
- Ren, D., Navarro, B., Xu, H., Yue, L., Shi, Q., and Clapham, D.E. (2001). A prokaryotic voltage-gated sodium channel. *Science* 294, 2372-2375.
- Shaya, D., Findeisen, F., Abderemane-Ali, F., Arrigoni, C., Wong, S., Nurva, S.R., Loussouarn, G., and Minor, D.L., Jr. (2014). Structure of a prokaryotic sodium channel pore reveals essential gating elements and an outer ion binding site common to eukaryotic channels. *J Mol Biol* 426, 467-483.
- Shaya, D., Kreir, M., Robbins, R.A., Wong, S., Hammon, J., Bruggemann, A., and Minor, D.L., Jr. (2011). Voltage-gated sodium channel (NaV) protein dissection creates a set of functional pore-only proteins. *Proc Natl Acad Sci U S A* 108, 12313-12318.
- Stein, R.A., Beth, A.H., and Hustedt, E.J. (2015). A Straightforward Approach to the Analysis of Double Electron-Electron Resonance Data. *Methods Enzymol* 563, 531-567.
- Strelkov, S.V., and Burkhard, P. (2002). Analysis of alpha-helical coiled coils with the program TWISTER reveals a structural mechanism for stutter compensation. *J Struct Biol* 137, 54-64.